*J. Fluid Mech.* (2013), *vol.* 726, *pp.* 338–370.  
doi:10.1017/jfm.2013.228

# Self-similar decay and mixing of a high-Schmidt-number passive scalar in an oscillating boundary layer in the intermittently turbulent regime

**Carlo Scalo[1],†, Ugo Piomelli[1] and Leon Boegman[2]**

[1]Department of Mechanical and Materials Engineering, Queen's University, 130 Stuart Street, Kingston, Ontario K7L 3N6, Canada

[2]Department of Civil Engineering, Queen's University, 58 University Avenue, Kingston, Ontario K7L 3N6, Canada

(Received 3 September 2012; revised 26 April 2013; accepted 28 April 2013)

We performed numerical simulations of dissolved oxygen (DO) transfer from a turbulent flow, driven by periodic boundary-layer turbulence in the intermittent regime, to underlying DO-absorbing organic sediment layers. A uniform initial distribution of oxygen is left to decay (with no re-aeration) as the turbulent transport supplies the sediment with oxygen from the outer layers to be absorbed. A very thin diffusive sublayer at the sediment–water interface (SWI), caused by the high Schmidt number of DO in water, limits the overall decay rate. A decomposition of the instantaneous decaying turbulent scalar field is proposed, which results in the development of similarity solutions that collapse the data in time. The decomposition is then tested against the governing equations, leading to a rigorous procedure for the extraction of an ergodic turbulent scalar field. The latter is composed of a statistically periodic and a steady non-decaying field. Temporal averaging is used in lieu of ensemble averaging to evaluate flow statistics, allowing the investigation of turbulent mixing dynamics from a single flow realization. In spite of the highly unsteady state of turbulence, the monotonically decaying component is surprisingly consistent with experimental and numerical correlations valid for steady high-Schmidt-number turbulent mass transfer. Linearly superimposed onto it is the statistically periodic component, which incorporates all the features of the non-equilibrium state of turbulence. It is modulated by the evolution of the turbulent coherent structures driven by the oscillating boundary layer in the intermittent regime, which are responsible for the violent turbulent production mechanisms. These cause, in turn, a rapid increase of the turbulent mass flux at the edge of the diffusive sublayer. This outer-layer forcing mechanism drives a periodic accumulation of high scalar concentration levels in the near-wall region. The resulting modulated scalar flux across the SWI is delayed by a quarter of a cycle with respect to the wall-shear stress, consistently with the non-equilibrium state of the turbulent mixing.

**Key words:** self-similarity, oscillating boundary layer, high-Schmidt-number mass transfer

† Present address: Center for Turbulence Research, NASA/Stanford University Mechanical Engineering & Institute for Computational Mathematical Engineering, Room 500V, Building 500, Stanford University, Stanford, CA 94305-30035, USA. Email address for correspondence: scalo@stanford.edu

## 1. Introduction

Oscillatory currents are frequently observed in marine environments (e.g. Trowbridge & Agrawal 1995) and are responsible for driving important transport processes that regulate the ecosystem balance. Dissolved oxygen (DO) transfer to organic sediment beds is one of them (e.g. Lorke *et al.* 2003) and is the focus of the present work. The presence of adequate DO concentrations (nominally above 2–4 mg $l^{-1}$) is critical for the survival of aquatic life in lakes and oceans. Agricultural runoff is the primary cause of low levels of oxygen (or 'hypoxia'). It transports excess nutrients to the water surface, spurring growth of plankton, which then dies and sinks to the bottom (sediment bed) where DO-consuming bacteria feed on it, causing near-bed hypoxia. Stratification, typically reaching its peak intensity over the summer, worsens this state by inhibiting mixing in the water column and reoxygenation of the bottom water layers. As a result, the oxygen budget there is largely governed by the DO flux to the sediment bed, commonly referred to as the sediment oxygen demand or uptake (SOU) (Bouldin 1968; Patterson, Allanson & Ivey 1985; Veenstra & Nolen 1991). For example, Hanes & Irvine (1968) have estimated that the SOU in certain rivers accounts for approximately 50 % of the total oxygen budget while Burns & Ross (1972) have found this to be 81 % for Lake Erie's central basin, which currently experiences oxygen depletion (Rao *et al.* 2008). Areas affected by high levels of hypoxia are known as 'dead zones' and have severe economical and environmental consequences (Committee on Environment and Natural Resources 2010). Dead zones can be found in highly populated coastal environments, including the Gulf of Mexico, the Pacific and the Atlantic coast of the US, Lake Erie, and the Baltic Sea (Diaz & Rosenberg 2008; Rabalais *et al.* 2010).

Oxygen dissolved in water behaves as a high-Schmidt-number passive scalar with molecular diffusivity typically three orders of magnitude lower than the water kinematic viscosity. The persistence of scalar fluctuation gradients below the Kolmogorov scale and within the viscous sublayer (in the case of turbulent mass transfer to a wall) poses significant challenges. Field-scale, experimental and numerical studies have shown that in a statistically steady (equilibrium) flow, for example, the DO transfer rate across the sediment–water interface (SWI) can only be predicted by taking into account turbulent velocity fluctuations in the viscous sublayer (Hanratty 1956; Pinczewski & Sideman 1974; Campbell & Hanratty 1983; Lorke *et al.* 2003; Scalo, Piomelli & Boegman 2012*a*). Simple semi-empirical laws such as the one by Shaw & Hanratty (1977) have proven to predict successfully the mass-transfer rate in such conditions. High-Schmidt-number mass transfer driven by an unsteady (non-equilibrium) turbulent flow is expected to pose significant challenges from a modelling perspective and is the focus of the present study.

Oscillatory currents occur in nature over a wide range of frequencies and amplitudes. Periods of oscillation can range from the order of a day (basin-scale seiches, tidal motions) to minutes (nonlinear waves propagating on stratified layers), usually corresponding, respectively, to current intensities of the order of 1 cm $s^{-1}$ and 1 m $s^{-1}$. We focus here on the idealized case of a uniform, monochromatic, zero-mean free-stream current bounded only on one side by a smooth flat wall. In this case the flow regime is uniquely determined by the Reynolds number $Re_{\delta_s} = U^*_{om}\delta^*_s/\nu^*$ based on the Stokes thickness $\delta^*_s = \sqrt{2\,\nu^*/\omega^*}$, where $\nu^*$ is the kinematic viscosity and $\omega^* = 2\pi/T^*$ ($T^*$ is the period of the forcing), and on the free stream current amplitude $U^*_{om}$. In the present work the free-stream current is expressed as $U^*_\infty = U^*_{om}\sin(\phi)$, where $\phi = \omega^* t^*$ is the phase angle. All starred quantities are dimensional.

Since the early numerical simulations and laboratory experiments by Hino *et al.* (1983), Spalart & Baldwin (1989), Sleath (1987), Jensen, Sumer & Fredsøe (1989), Akhavan, Kamm & Shapiro (1991*b*,*a*) the different flow regimes have been identified as: (i) the fully laminar regime, for $Re_{\delta_s} < 100$; (ii) the disturbed laminar regime, where small-amplitude perturbations are visible but do not transition to turbulence, for $100 < Re_{\delta_s} < 550$; (iii) the intermittently turbulent (IT) regime, for $500 < Re_{\delta_s} < 1800$; (iv) the fully turbulent (FT) for $Re_{\delta_s} > 1800$. The lower limit for the presence of well-developed turbulence with a smooth wall ($Re_{\delta_s} = 500-600$) is defined by the existence of a logarithmic layer and regular Reynolds stress anisotropy. For higher Reynolds numbers, in the IT regime, turbulent kinetic energy (TKE) production is sustained and generated periodically during the cycle. Favourable pressure gradient effects during the acceleration phase, $0° < \phi < 90°$, freeze TKE production mechanisms (even at high Reynolds numbers), while turbulent diffusion transports the near-wall turbulence (generated in the previous decelerating phase) in the outer layer. In the following deceleration stage, $90° < \phi < 180°$ low-speed streaks start to appear close to the wall and rapidly become unstable generating a local maximum in the wall-shear stress and turbulence production, with well-developed turbulence sustained in the near-wall region until flow reversal (Verzicco & Vittori 1996; Vittori & Verzicco 1998; Costamagna, Vittori & Blondeaux 2003), analogously to the regenerative near-wall TKE cycle in a steady boundary layer (Jimenez & Pinelli 1999). As shown later, the passive scalar field is modulated by the periodic TKE production and diffusion cycle of the IT regime and, in the high-Schmidt-number limit, exhibits a non-trivial frequency response to the turbulent forcing. These non-equilibrium effects vanish for increasing $Re_{\delta_s}$, resulting in a reduction of the phase lag between the wall-shear stress and the free-stream oscillating current and an anticipated establishment of the log law in the deceleration phase. The FT regime is characterized by fully developed turbulence through most of the cycle and TKE budgets reveal a structure similar to that of an equilibrium boundary layer except at flow reversal.

A Reynolds number of $Re_{\delta_s} = 800$ has been chosen for the present work to emphasize the effects of the aforementioned periodic regeneration of turbulence while retaining phases of well-developed turbulence. The highly variable flow state poses significant challenges for subgrid-scale (SGS) modelling which starts to become reliable only in the upper limit of the IT regime (Salon, Armenio & Crise 2007), where fully developed turbulence has already appeared at $\phi = 60°$. A direct numerical resolution of all the turbulent velocity scales is, therefore, adopted in the present study while the subgrid-scale closure is retained only for the scalar field.

A similar approach was used by Wang & Lu (2004), who performed large-eddy simulations (LES) of heat transfer in a pulsating channel for Prandtl numbers up to $Pr = 100$. It was found that, for high Prandtl numbers, the important mechanisms regulating the heat transfer occur primarily in a very thin region close to the wall (diffusive and/or thermal buffer layers) and that temperature fluctuations rapidly decay away from the wall. This result is confirmed in the present study, and an explanation based on the size of the resolved outer-layer coherent structures, which control the scalar entrainment, is provided.

The first field study to correlate directly the state of near-wall turbulence with the rate of DO transfer across the SWI was by Lorke *et al.* (2003) who relied on DO measurements taken in an oscillating bottom boundary layer in Lake Alpnach (Switzerland) driven by an 18 h period current. They observed a phase lag between the SOU, the near-wall turbulent dissipation rate and free-stream current intensity revealing non-equilibrium effects at a geophysical scale. Bryant *et al.* (2010)

performed a similar investigation in the same lake, capturing the occurrence of an almost complete laminarization of the near-bed region close to flow reversal and the subsequent retransition towards a fully turbulent state in an 8 h oscillating flow. A large excursion of the SOU was observed. Scalo, Boegman & Piomelli (2013) reproduced the field measurements by Bryant *et al.* (2010) in an idealized open-channel setup showing that the long geophysical scales associated with the oscillating flow still allow equilibrium mass-transfer models to predict the SOU accurately.

In the present paper we investigate the transient decay of DO in an oscillating boundary layer in the IT regime, where periodically regenerating turbulence drives the DO transport towards an underlying mass-absorbing sediment layer. Re-aeration from the top boundary is prevented to simulate the reduced turbulent flux across the stratified region, or thermocline. The goal is to investigate oxygen depletion dynamics in the hypolimnetic layers of water bodies (the non-stratified region below the thermocline), extending the analysis of Scalo *et al.* (2013) to fully non-equilibrium conditions. As shown by Gayen, Sarkar & Taylor (2010), Stokes–Reynolds numbers in the IT regime, $Re_{\delta_s} = 1800$ in their case, can be observed in geophysical flows despite the typically long time scales of oscillatory currents in water bodies. The goal of the present study is to investigate the fundamental transport mechanisms in the IT regime. The choice of a lower Reynolds number, $Re_{\delta_s} = 800$, highlights the key features of non-equilibrium turbulence.

In the following, we begin by describing the mathematical and numerical methods used for the transport on the water side and in the sediment layer. A triple decomposition of the decaying turbulent scalar field and collapse of the data on similarity solutions is obtained through appropriate manipulation of the governing equations. Turbulent mixing dynamics are investigated by extracting a non-decaying, statistically periodic (ergodic) turbulent scalar field from the only available flow realization, and exploiting the newly derived self-similar scaling.

## 2. Problem formulation

A direct numerical simulation (DNS) approach for the velocity field is adopted to capture accurately the highly transitional and intermittent nature of the low-Reynolds-number flow, while the effects of unresolved sub-Kolmogorov scales in the DO are accounted for by a subgrid-scale (SGS) closure.

The flow is incompressible and driven by a sinusoidal free-stream current of amplitude $U^*_{om}$ and period $T^* = 2\pi/\omega^*$, where $\omega^*$ is the angular frequency of the oscillation. The dimensionless conservation equations for mass and momentum are

$$\frac{\partial u_i}{\partial x_i} = 0, \tag{2.1}$$

$$\frac{\partial u_j}{\partial t} + \frac{\partial u_i u_j}{\partial x_i} = -\frac{\partial p}{\partial x_j} + \frac{1}{Re_{\delta_s}}\nabla^2 u_j + \frac{2}{Re_{\delta_s}}\cos(\omega t)\delta_{1j}, \tag{2.2}$$

where $x_1, x_2$ and $x_3$ (or $x, y$ and $z$) are, respectively, the streamwise, wall-normal and spanwise coordinates, $u_i$ the velocity components in those directions, and $p$ the normalized pressure. These equations have been made dimensionless by using the Stokes thickness $\delta^*_s = \sqrt{2\,\nu^*/\omega^*}$, where $\nu^*$ is the kinematic viscosity of water, and the free-stream current amplitude $U^*_{om}$ as the reference length and velocity scale, respectively. The Reynolds number is therefore defined as $Re_{\delta_s} = U^*_{om}\delta^*_s/\nu^*$, and the normalized space and time coordinates as $x_i = x^*_i/\delta_s$ and $t = t^* U^*_{om}/\delta^*_s$. All starred quantities are dimensional and their dimensionless counterparts are unstarred.

The filtered equation for the DO transport on the water side (above the sediment bed) is

$$\frac{\partial \overline{c}}{\partial t} + \frac{\partial \overline{u}_i \overline{c}}{\partial x_i} = \frac{\partial}{\partial x_i}\left[\frac{1}{Sc\, Re_{\delta_s}}\frac{\partial \overline{c}}{\partial x_i} - J_i^{sgs}\right], \tag{2.3}$$

where $Sc = \nu^*/D^*$ is the Schmidt number, $D^*$ the molecular diffusivity of oxygen in water and $\overline{c}$ the instantaneous filtered scalar field normalized by the free-stream DO concentration, $C^*_\infty$, at the beginning of the simulation.

The SGS scalar flux, $J_i^{sgs}$, is the result of a filtering operation and is parameterized by a dynamic eddy-diffusivity model. The primary filter width is equal to $\overline{\Delta} = (\Delta_1\Delta_2\Delta_3)^{1/3}$ where $\Delta_i$ is the grid spacing along the $i$th spatial coordinate. The dynamic procedure (Germano *et al.* 1991; Lilly 1992) adopted requires the explicit application of a secondary (test) filter, which is the combination of three one-dimensional three-point top-hat discrete filters with filter width equal to $\sqrt{6}\overline{\Delta}$. The extension of the dynamic model to the scalar transport at high Schmidt numbers has been shown to be accurate by Zang, Street & Koseff (1993), Calmet & Magnaudet (1997) and Na (2004).

The normalized instantaneous DO concentration level in the sediment layer, $c_s$, is determined by more complex mechanisms. Dissolved oxygen is diffused but also depleted by decomposing organic matter. The governing equation for $c_s$ is

$$\frac{\partial c_s}{\partial t} = \frac{\partial}{\partial x_i}\left[\frac{F(\varphi)}{Sc\, Re_{\delta_s}}\frac{\partial c_s}{\partial x_i}\right] - \dot{c}_s, \tag{2.4}$$

where $F(\varphi)$ is a function of the sediment porosity $\varphi$, which accounts for reduction of the molecular diffusivity in the pore water. A commonly used approximation for this function is $F(\varphi) = \varphi^2$ for $\varphi < 0.7$. It is possible to retrieve the value of the sediment porosity from the slope discontinuity in measured mean oxygen profiles at the SWI (Røy, Huettel & Joergensen 2004). Solutes in the pore water are also, in general, advected and dispersed through the porous medium but these processes can be neglected for smooth, flat and cohesive (rich in organic matter) beds. A thorough discussion on the modelling of solute transport in the sediment bed can be found in Boudreau & Jørgensen (2001), O'Connor & Hondzo (2007), Higashino *et al.* (2008), Higashino, Clark & Stefan (2009) and Higashino & Stefan (2011) and numerical modelling issues on the coupling with water-side eddy-resolving models in Scalo, Piomelli & Boegman (2012*b*). For the present work, dispersion and mean advection effects will be ignored. The sediment layer is a boundary condition for the water-side turbulent transport, which is our main focus.

The DO absorption by organic matter is represented by the nonlinear sink term, $\dot{c}_s$, which is modelled as (Higashino *et al.* 2008)

$$\dot{c}_s = \chi \frac{c_s}{K_{O_2} + c_s}, \tag{2.5}$$

where

$$\chi = \frac{\chi^* \mu^*}{Y_c}\frac{\delta_s^*}{U^*_{om}\, C^*_\infty}. \tag{2.6}$$

The parameters used in (2.6) are: $\mu^*$, maximum specific DO utilization rate (in day$^{-1}$); $K^*_{O_2}$, half-saturation coefficient for DO utilization (in mg l$^{-1}$); $Y_c$, effective yield for the microbial utilization of DO; and $\chi^*$ (in mg l$^{-1}$), the concentration of DO-absorbing

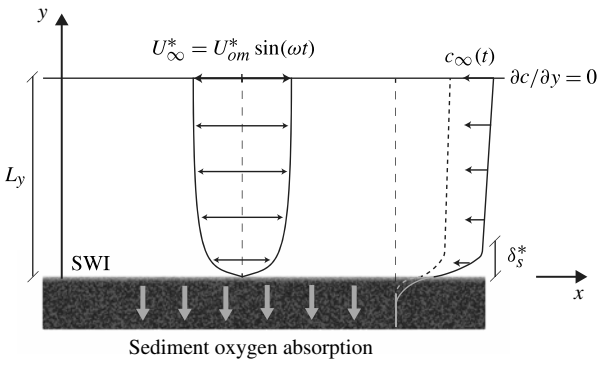


FIGURE 1. Computational setup for oxygen absorption driven in an oscillating boundary layer. The thickness of the diffusive sublayer is exaggerated and the shape of the velocity profiles simplified for visualization purposes. The spanwise direction ($z$) is omitted in the figure.

| $\mu^*$ (day$^{-1}$) | $K^*_{O_2}$ (mg l$^{-1}$) | $Y_c$ | $\chi^*$ (mg l$^{-1}$) | $C^*_\infty$ (mg l$^{-1}$) | $\varphi$ |
|---|---|---|---|---|---|
| 2.4 | 0.2 | 1 | 100–700 | 12 | 0.55 |

TABLE 1. Sediment-layer bio-geochemical parameters.

bacteria populating the sediment bed, not directly measurable. The validation of the complete oxygen transport and absorption model against laboratory experiments (O'Connor & Hondzo 2008) can be found in Scalo *et al.* (2012*b*).

All of the aforementioned bio-geochemical parameters are set as constants in the model (table 1). An improved DO transport and absorption model in the sediment layer could be adopted by taking into account, for example, variations of bio-geochemical parameters with depth. However, such distributions are not typically known *a priori*, or easily measurable, and any particular choice would be arbitrary or problem specific. Moreover, the influence of such parameters on the transport is localized; the near-wall water transport dynamics are affected primarily by the bio-geochemical composition of the superficial layers of the sediment bed (Scalo *et al.* 2012*b*). Taking into account the variability with depth is, therefore, not expected to alter the nature of turbulent mixing on the water side, which is the focus of the present study. A uniform distribution of organic matter, consistent with the assumption of uniform porosity and permeability, will be adopted.

## 3. Computational setup

The computational setup used is shown in figure 1. The governing equations (2.1) and (2.2) are solved in a Cartesian domain. In the streamwise and spanwise directions, $x$ and $z$, periodic boundary conditions are used for all quantities. The velocity obeys no-slip conditions at the lower wall and free-slip conditions at the top boundary; for the scalar we use Neumann conditions, i.e. assigned mass flux at the bottom wall, derived from the solution of (2.4) (see Scalo *et al.* 2012*b*). The oxygen flux from

| $Re_{\delta_s}$ | $L_x \times L_y \times L_z$ | $N_x \times N_y \times N_z$ | $\Delta x^+$ | $\Delta z^+$ | $\Delta y^+_{max}$ | $Sc$ |
|---|---|---|---|---|---|---|
| 800 | $150 \times 13\pi \times 25$ | $1024 \times 384 \times 256$ | 1–6 | 0.6–4 | 0.2–12 | 1020 |

TABLE 2. Simulation parameters used for both low- and high-absorption cases.

the top boundary is set to zero via homogeneous Neumann conditions (no re-aeration) resulting in a decaying turbulent scalar field.

The numerical model used to compute the flow on the water side is a well-validated finite-difference code (Keating *et al.* 2004), based on a staggered grid. Second-order central differences are used for both convective and diffusive terms. The time advancement scheme is a Crank–Nicolson scheme for the wall-normal diffusive term, and a low-storage three-step second-order Runge–Kutta method for the other terms. The solution of the Poisson equation is obtained by Fourier transform of the equation in the spanwise and streamwise directions, followed by a direct solution of the resulting tridiagonal matrix, at each wavenumber. The code is parallelized using the MPI protocol. The equations in the sediment layer are solved with the same numerical approach as the one adopted for the water side and have the same accuracy and stability properties. The results for the velocity field have been validated against the DNS of Moser, Kim & Mansour (1999) in the channel flow configuration and the experimental data by Jensen *et al.* (1989) for the present setup.

We performed DNS of the velocity field and LES for the scalar field for $Re_{\delta_s} = 800$ and $Sc = 1020$ (corresponding to water temperature of 8°C and dissolved oxygen saturation levels of $C^*_\infty = 12$ mg l$^{-1}$). Two different bacterial populations have been tested, $\chi^* = 100$ and 700 mg l$^{-1}$, resulting in different boundary conditions (i.e. absorption rates) for the oxygen field. In all cases, the decaying oxygen field is initialized with a uniform distribution equal to the reference value and a completely anoxic sediment layer. The initial velocity field is taken from an independent, fully converged simulation carried out on the same grid without the scalar field. The domain size has been chosen to accommodate the large structures, the near-wall streaks and the elongated concentration patches at the SWI (Scalo *et al.* 2012*a*). Also, a very large computational domain has the advantage of reducing the variance of plane-averaged statistics, used in the present study to investigate the statistical transient. The grid size has been chosen accordingly to resolve the diffusive sublayer thickness, to maintain DNS resolution for the velocity field and to model exclusively the sub-Kolmogorov scales of the concentration field. This approach has been successfully used in Bergant & Tiselj (2007) and Scalo *et al.* (2012*a*) to simulate high-Schmidt-number mass-transfer problems. It is stressed, in particular, that mean profiles and turbulent fluxes are very accurately predicted even on coarse grids. All the parameters used are summarized in table 2.

## 4. Self-similar decay and triple solution decomposition

### 4.1. *Definition of spatial, temporal and statistical averaging operators*

The data set available for the present study is one realization of a decaying scalar field in a turbulent flow. Several analogous statistically independent numerical experiments would have to be performed to evaluate directly ensemble averages of the scalar field (i.e. averaging along planes parallel to the wall and over different simulations at a given time). A triple solution decomposition is proposed that will allow the extraction

of an ergodic component from the decaying turbulent scalar field, removing such limitation. We define in this section the averaging operators used for such a derivation.

From a statistical point of view the artificially generated turbulence can be regarded as a collection of stochastic processes (one for every $y$) unfolding in space ($x$, $z$) and time ($t$). Letting $W^k(x, z; t)$ be the $k$th realization of a process of this sort, the statistical- or ensemble-average operator

$$\langle W^k \rangle = \lim_{N_k \to \infty} \frac{1}{N_k} \sum_{k=0}^{N_k} W^k(x, z; t) \tag{4.1}$$

returns the statistical expectation of $W$ for every $x$, $z$ and $t$. For the present data only one flow realization is available and only spatial and temporal averages can be directly evaluated. These are the phase-average, plane-average, and time-average operators, respectively

$$\left.\begin{aligned} \langle W^k \rangle_\phi &= \frac{1}{N_\phi} \sum_{i=0}^{N_\phi} W^k(x, z; t + T/2\pi(\phi + \mathrm{i}\pi)), \\ \langle W^k \rangle_{xz} &= \frac{1}{L_x L_z} \int_0^{L_x} \int_0^{L_z} W^k(x, z; t)\, \mathrm{d}x\, \mathrm{d}z, \\ \overline{W^k}^{\Delta T} &= \frac{1}{\Delta T} \int_t^{t+\Delta T} W^k(x, z; \tau)\, \mathrm{d}\tau, \end{aligned}\right\}. \tag{4.2}$$

where $\phi$ is the phase angle, $N_\phi$ the number of semi-cycles available for averaging and $\Delta T$ is the extent of the time-averaging window.

If $W^k$ is statistically periodic in time, the ensemble- and phase-average operators converge to the same value for $N_\phi \to \infty$. If the process $W^k$ is statistically homogeneous in $x$ and $z$ then the plane-average operator will converge for a sufficiently large domain ($L_x \to \infty$ and $L_z \to \infty$) to the statistical average. For the data set used here, the plane-average operator is absorbed by both the phase-average operator, $\langle \langle \cdot \rangle_{xz} \rangle_\phi = \langle \cdot \rangle_\phi$, and the ensemble-average one, $\langle \langle \cdot \rangle_{xz} \rangle = \langle \cdot \rangle$. Only one realization of the flow is present so the superscript $k$ will be dropped for the flow variables in the following derivations.

### 4.2. *Visual inspection of time series of plane averages*

While the passive scalar field experiences a transient decay, the underlying turbulent velocity field, driving the turbulent scalar mixing, undergoes a statistically quasi-periodic regenerative cycle. As stated in the introduction, turbulent coherent structures are generated in the near-wall region and released in the outer layer during the deceleration phase, periodically sustaining the turbulent production cycle. Inspection of the transient data reveals the expected signature of this periodic modulation on the scalar field overlapping a background monotonic decay.

Figure 2 shows time series of plane-averaged oxygen concentration at the top boundary ($y = L_y$), which is indicative of a monotonically decaying component in the mean scalar field. The total decay rate is approximately 2 % over 20 cycles for the highly absorbing case. A steady decay rate can be observed at all distances from the wall (figure 3) with rate of decay increasing with $y$.

Coherent oscillations with period $T/2$ can be observed in the plane-averaged time series and are dominant in the fully mixed region ($y < 15$). The evolution of turbulent coherent structures in the IT regime is responsible for such modulation of the scalar

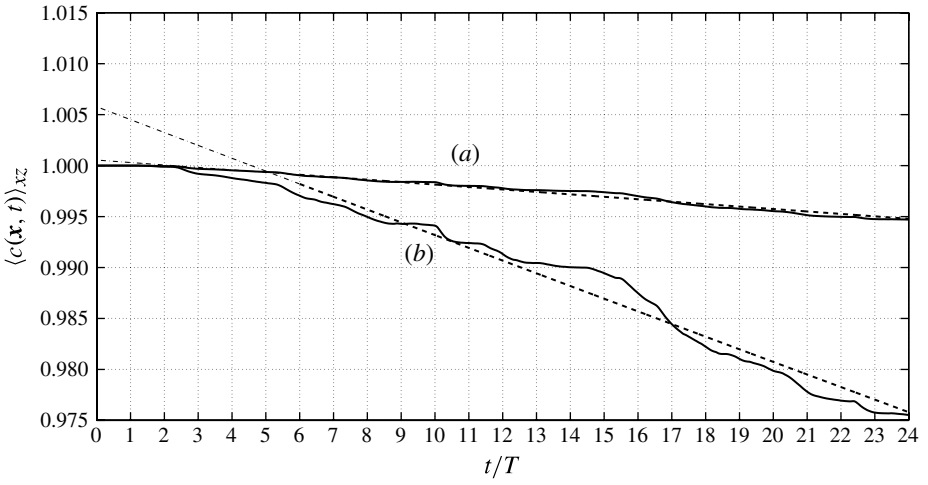


FIGURE 2. Plane-averaged free-stream oxygen concentration: $\langle c(\boldsymbol{x}, t)\rangle_{xz}$ at $y = L_y$ (——) for $\chi^* = 100$ mg l$^{-1}$ ($a$) and $\chi^* = 700$ mg l$^{-1}$ ($b$), and mean decay trend obtained by fitting over $t > 6T$ (– – –) (see text).

field. For $y > 15$ traces of coherent oscillations are lost and the turbulent mixing and entrainment can be regarded as statistically steady (see discussion in § 8).

Traces of the fluctuating component of the instantaneous scalar field are still visible in figures 2 and 3. The large computational domain (table 2) and the relatively low resolved variance of the high-Schmidt-number scalar allow the plane-average operator to filter out the spatial modes of the stochastic component of the field. However, well defined low-amplitude and low-frequency deviations of the plane-averaged oxygen concentration from the mean decay trend (for now, only qualitatively determined) are still visible at all distances from the wall and persist over several oscillation periods. These resemble anomalous features observed in time series of passive scalars such as the ramp–cliff structures (Warhaft 2000), which are typically amplified in the case of a high-Schmidt-number contaminant (Antonia & Orlandi 2003) and are also present in fully turbulent, steady flows. Their persistence in spatially averaged signals and their very long characteristic time scales – approximately one order of magnitude larger than the oscillating forcing periodic – suggest that they are a non-coherent, fluctuating component of the turbulent scalar field. Consistently with this interpretation, these fluctuations become more significant in simulations with smaller computational domains, which show a well-defined intermittent pattern (discussed in § 7) and can only be removed by averaging over statistically independent experiments.

### 4.3. *Self-similar hypothesis and solution decomposition*

A rigorous definition of the monotonically decaying, oscillating and stochastic component of the scalar field, only conceptually introduced in the previous section, is provided here based on collapsing via similarity solutions.

An initial transient evolution of the oxygen levels is visible at all distances from the SWI and, in particular, for $y < 1$. This is due to the long time scales of adjustment of the bacterial absorption, in the initially anoxic sediment layer, to the mass flux imposed across the SWI from the water-side turbulence. After approximately 6 cycles

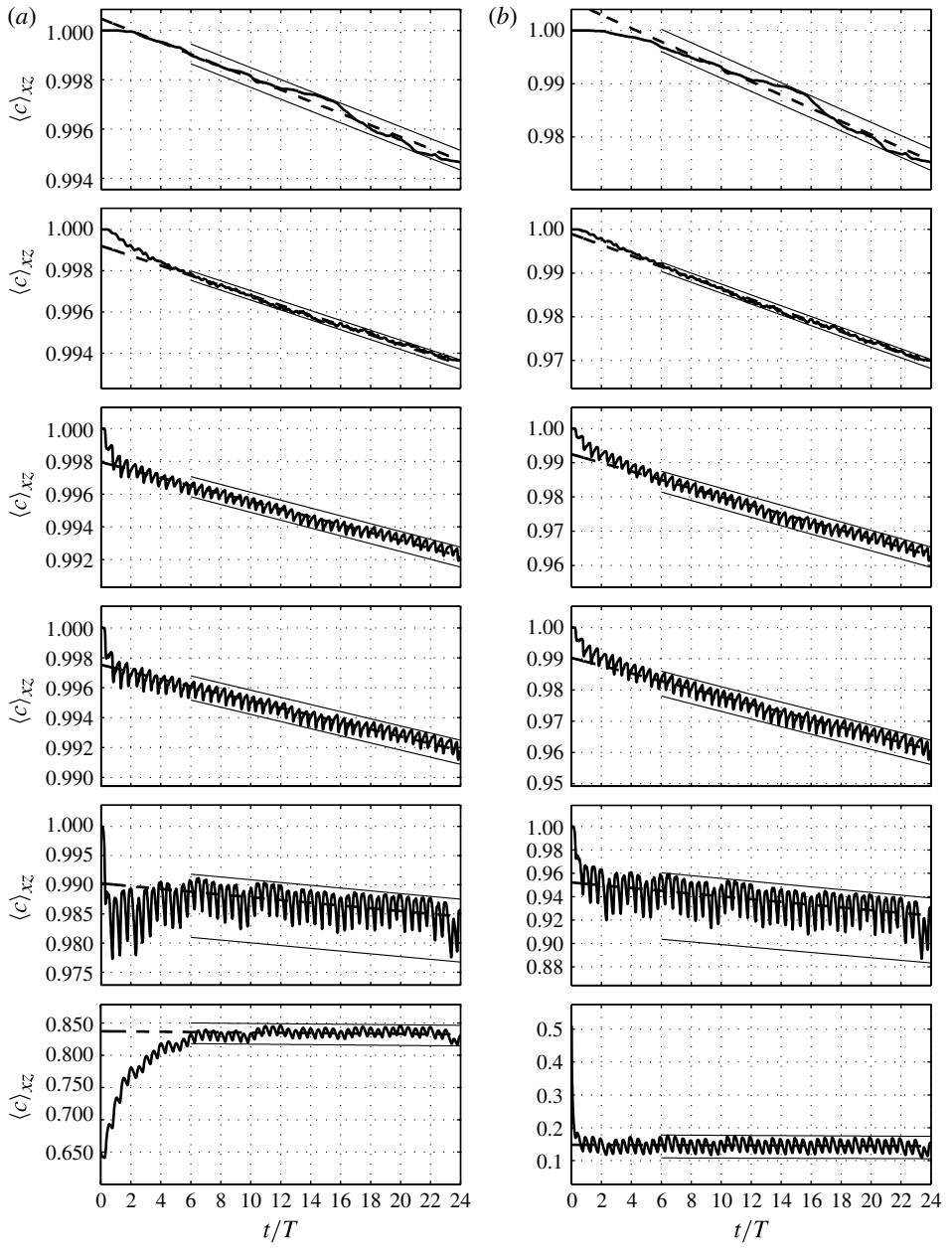


FIGURE 3. Time series of plane-averaged oxygen concentration for $y = 0$, 0.1, 0.5, 1, 15 and 40 (from bottom to top) and $\chi^* = 100\ \mathrm{mg\,l^{-1}}$ (*a*) and $\chi^* = 700\ \mathrm{mg\,l^{-1}}$ (*b*). Non-oscillating/steady transient decay and fitting over $t > 6T$ (– – –) (see text). Signals bounded on both sides by envelope (——) with amplitude decaying proportionally to $d(t)$.

a dynamical equilibrium is reached and the oxygen distribution exhibits a well-defined pattern of decay. A preliminary fitting is carried out for all $y$ over $t > 6T$ (figure 3), suggesting the following functional form for the non-oscillating decaying component

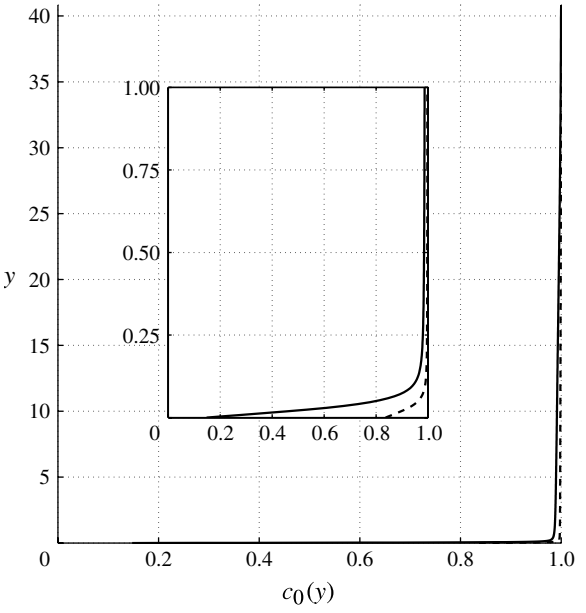


FIGURE 4. Profiles of $c_0(y)$ for $\chi^* = 100$ mg l$^{-1}$ (– – –) and $\chi^* = 700$ mg l$^{-1}$ (——); the inset figure highlights the near-wall ($0 < y < 1$) concentration boundary layer.

of the ensemble-average oxygen distribution:

$$C(y, t) = c_0(y)d(t), \tag{4.3}$$

where $C(y, t) = \langle c(\boldsymbol{x}, t)\rangle$ and $d(t)$ is a positive, dimensionless, monotonically decaying function of time obtained by least-square fitting the plane-averaged oxygen distribution at $y = L_y$ with a (for now) first-order polynomial in time (figure 2). The coefficient $c_0(y)$ is set to 1 at $y = L_y$ and determined for every other $y < L_y$ by minimizing the norm of

$$|\langle c(\boldsymbol{x}, t)\rangle_{xz} - c_0(y)d(t)| \tag{4.4}$$

over $t > 6T$.

In spite of the approximations made, the resulting profiles of $c_0(y)$ (figure 4) closely resemble the shape of an ensemble-averaged decaying mean oxygen distribution in a statistically steady turbulent open channel flow, with zero-mass-flux conditions at the top boundary and an absorbing sediment layer at the bottom boundary. This is the first evidence supporting the existence of a self-similar structure in the decaying mean oxygen field, where $c_0(y)$ represents the statistical average of the steady ergodic component of the scalar field. More rigorous derivations (carried out in § 5) will show that the linear approximation used for $d(t)$ is accurate over the time frame analysed.

As previously mentioned, sufficiently far away from the turbulent bottom boundary layer, the plane-averaged oxygen concentration loses trace of the harmonic forcing, exposing the aforementioned low-amplitude/low-frequency stochastic component. Its amplitude is negligible on large computational domains (such as the one used here). The deviation of the ensemble-averaged free-stream (decaying) oxygen concentration,

$$c_\infty(t) \equiv \langle c(\boldsymbol{x}, t)\rangle, \tag{4.5}$$

from the one-time plane average $\langle c(\boldsymbol{x},t)\rangle_{xz}$ at $y=L_y$ is expected to be small (see discussion in § 7). Fitting the plane-averaged time series at $y=L_y$ with the correct functional form for $d(t)$, over a sufficiently long time interval, will, therefore, return values very close to the ensemble average (4.5). The relationships (4.3) and (4.5), together with the choice of $c_0(y=L_y)=1$, imply that

$$c_\infty(t)=d(t) \tag{4.6}$$

over the time range of self-similarity.

The signature of the statistically periodic forcing in the scalar field evolution is remarkably pronounced suggesting that the passive scalar field acts as a linear system forced by a periodic turbulent flux (see § 8.2). The nonlinearities introduced by the SGS modelling term in (2.3), which is meant to model the linear residual mixing term, are not expected to affect significantly the mean flow dynamics, especially at the grid resolution adopted in the present study. We therefore hypothesize that, in the self-similar range, the ensemble-averaged concentration field contains a coherent oscillating component, $\widetilde{C}(y,t)$, linearly overlapping the mean monotonic decay (4.3), such that

$$\langle c(\boldsymbol{x},t)\rangle = C(y,t)+\widetilde{C}(y,t). \tag{4.7}$$

Without loss of generality, $\widetilde{C}(y,t)$ can be rewritten as

$$\widetilde{C}(y,t)\equiv \widetilde{d}(y,t)\widetilde{c}_0(y,\phi), \tag{4.8}$$

where $\widetilde{d}(y,t)$ is a non-oscillating dimensionless function chosen, for every $y$ and $t$, to enforce the periodicity of $\widetilde{c}_0(y,\phi)$, and $\phi$ is the phase angle (every function of $\phi$ is intended hereafter as periodic with period $T/2$). In particular, the least-square fitting procedure adopted to derive (4.3) implies that

$$\overline{\widetilde{c}_0(y,\phi)}^{T/2}=0, \tag{4.9}$$

where the time-average operator (4.2) with a time window of $\Delta T=T/2$ has been used. None of the quantities in (4.8) and (4.7) is stochastic; therefore, they do not include the irregular low-amplitude/low-frequency fluctuations discussed in § 4.2. With the introduction of (4.8) we extend the idea of self-similarity to the oscillating component of the mean-oxygen distribution, without excluding the possibility of a different decay rate (or no decay at all).

A visual inspection of the data in figure 3 provides no elements to anticipate the functional form of $\widetilde{d}(y,t)$. The solid lines bounding the times series suggest that there might either be no decay of $\widetilde{C}(y,t)$ (i.e. $\widetilde{d}(y,t)=$ const) or that $\widetilde{d}(y,t)$ decays with time scales similar to $d(t)$. However, no further assumptions on $\widetilde{d}(y,t)$ are required to proceed in our analysis.

The decomposition (4.7) can now be extended to the instantaneous scalar field by including a stochastic component. The latter can be simply recovered as the remainder of the ensemble-averaging operator

$$C'(\boldsymbol{x},t)=c(\boldsymbol{x},t)-\langle c(\boldsymbol{x},t)\rangle. \tag{4.10}$$

It accounts for the aforementioned low-amplitude irregular fluctuations and, most importantly, the effects of the three-dimensional turbulent mixing (governed by turbulent structures), which is responsible for the observed shape of the mean profiles (figure 4) and for the modulation of the oscillating component $\widetilde{C}(y,t)$. The

introduction of (4.10) suggest the following form of the decomposition:

$$c(\boldsymbol{x}, t) = C(y, t) + \widetilde{C}(y, t) + C'(\boldsymbol{x}, t). \tag{4.11}$$

For the current computational setup, the statistical distribution of $C'(\boldsymbol{x}, t)$ is necessarily homogeneous in the streamwise and spanwise directions. However, there is no evidence to support that it is also periodic in time. Let us introduce another unknown function, $f(y, t)$, such that

$$C'(\boldsymbol{x}, t) = f(y, t)c_0'(\boldsymbol{x}, t), \tag{4.12}$$

where, by definition, $c_0'(\boldsymbol{x}, t)$ is a random variable with a statistically periodic probability distribution (with period $T/2$). While the spatial variability of $f$ has been restricted to $y$, the flow being statistically non-homogeneous only in the wall-normal direction (and time), to retain complete generality in the decomposition (4.12), from a statistical standpoint, $f(y, t)$ should also be a stochastic process, for every $y$, unfolding in time. However, given the obvious presence of a periodic component in the scalar field evolution – which can only be the result of statistically periodic turbulent mixing events, therefore, necessarily involving $C'(\boldsymbol{x}, t)$ – and the fact that the passive scalar fluctuations are created and sustained by a statistically periodic turbulent velocity field with time scales much shorter than the bulk concentration decay rate, it is safe to assume that $C'(\boldsymbol{x}, t)$ naturally contains a periodic component. This implies that $f(y, t)$ does not need to be stochastic. These considerations imply that

$$\langle v'(\boldsymbol{x}, t)c_0'(\boldsymbol{x}, t)\rangle = \langle v'(\boldsymbol{x}, t + T/2)c_0'(\boldsymbol{x}, t + T/2)\rangle = \langle v'(\boldsymbol{x}, t)c_0'(\boldsymbol{x}, t)\rangle_{\phi}. \tag{4.13}$$

Substituting (4.3), (4.8) and (4.12) into (4.11) yields the final form of the self-similar decay model for the instantaneous concentration field:

$$c(\boldsymbol{x}, t) = d(t)c_0(y) + \widetilde{d}(y, t)\widetilde{c}_0(y, \phi) + f(y, t)c_0'(\boldsymbol{x}, t), \tag{4.14}$$

illustrated in figure 5.

In § 5, the mathematical implications of the assumptions made so far are explored and solutions of the form (4.14) are tested against the governing equations and the numerical data. It is shown that $d(t)$, $\widetilde{d}(y, t)$ and $f(y, t)$ are all equal to the same exponentially decaying function of time and are independent of $y$. In § 6 the companion scalar variance budgets for $c_0(y)$ and $\widetilde{c}_0(y, \phi)$ are derived, confirming, from a statistical perspective, the interpretation of the latter quantities as the ensemble averages of two ergodic turbulent scalar fields. In § 7 the effects of the domain size and Schmidt number for the decaying scalar field are investigated, allowing extension of the validity of the decomposition (4.14) to lower Schmidt numbers and discussion of the effects of outer-layer and near-wall turbulent coherent structures on the mean decay rate. In § 8 statistics are finally extracted and the mixing dynamics are analysed.

As shown in figures 3 and 4 the only difference between the low and the high absorption cases is the overall rate of decay. Both are in full agreement with the considerations that have lead to the self-similar formulation (4.14). Therefore, for the sake of conciseness, only data from the high absorption case ($\chi^* = 700$ mg l$^{-1}$) are shown in the following.

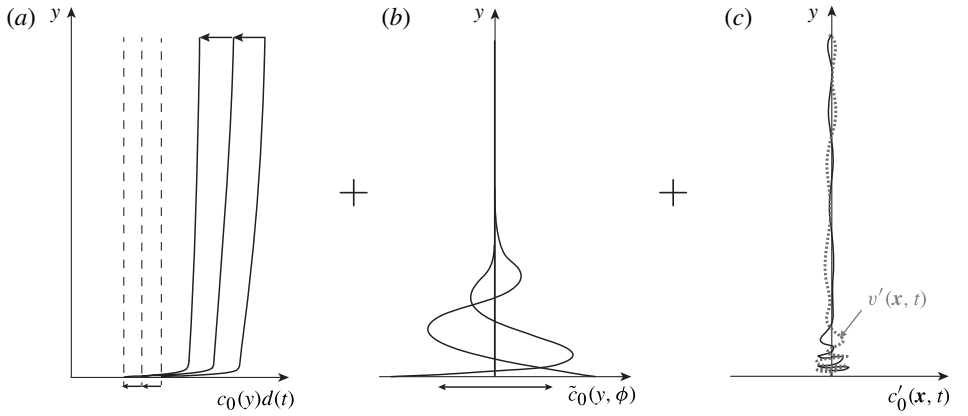


FIGURE 5. Illustration of the components in the decomposition (4.14). (*a*) Monotonically decaying component of the oxygen concentration field, $C(y,t) = c_0(y)d(t)$, with dashed lines indicating the corresponding value at the sediment–water interface; (*b*) coherent oscillating component, $\widetilde{c}_0(y,\phi)$; (*c*) statistically periodic stochastic component, $c_0'(\boldsymbol{x},t)$, correlated with turbulent velocity fluctuations, $v'(\boldsymbol{x},t)$ (dotted line). The decay is shown only for the non-oscillating mean component and is indicated by the arrows.

## 5. Decay law as an implication of self-similarity

Substituting (4.14) into (2.3), applying the ensemble-average operator and dividing by $d(t)$ yields

$$\begin{aligned}\frac{\mathrm{d}}{\mathrm{d}t}\log\left(d(t)\right)c_0(y) + \frac{1}{d(t)}\left(\frac{\partial}{\partial t}\widetilde{d}(y,t)\right)\widetilde{c}_0(y,\phi) + \frac{\widetilde{d}(y,t)}{d(t)}\frac{\partial}{\partial t}\widetilde{c}_0(y,\phi)\\ = -\frac{\partial}{\partial y}\left(\frac{f(y,t)}{d(t)}\overline{\langle v'c_0'\rangle_\phi}^{T/2}\right) - \frac{\partial}{\partial y}\left(\frac{f(y,t)}{d(t)}\widetilde{\langle v'c_0'\rangle_\phi}\right)\\ + \frac{1}{Re_{\delta_s}Sc}\frac{\mathrm{d}^2}{\mathrm{d}y^2}c_0(y) + \frac{1}{Re_{\delta_s}Sc}\frac{\mathrm{d}^2}{\mathrm{d}y^2}\left[\frac{\widetilde{d}(y,t)}{d(t)}\widetilde{c}_0(y,\phi)\right].\end{aligned} \tag{5.1}$$

The filtering symbol has been dropped for clarity and the subgrid-scale contribution has been omitted, as it would add unnecessary complications to the following derivations. The time-average operator applied over a semi-cycle $T/2$ has been used to decompose the resulting turbulent flux into a constant and a zero-mean periodic component:

$$\langle v'c_0'\rangle = \langle v'c_0'\rangle_\phi = \overline{\langle v'c_0'\rangle_\phi}^{T/2} + \widetilde{\langle v'c_0'\rangle_\phi}. \tag{5.2}$$

In the form (5.1), it is possible to discriminate the contributions to the overall mean concentration budget deriving from the different components in (4.14). For example, the steady self-similar diffusion term (third term on the right-hand side) can only be balanced by other constant, non-oscillating terms. The terms in (5.1) containing the periodic functions $\widetilde{c}_0(y,\phi)$ and $\widetilde{\langle v'c_0'\rangle_\phi}$ cannot add up to a constant function of time but, rather, to a periodic signal modulated by ratios of $d(t)$, $\widetilde{d}(y,t)$ and $f(y,t)$. Therefore, the only terms that could balance the steady diffusion term are the first term on the left-hand side, representing the steady, non-oscillating decay of oxygen concentration occurring at every $y$, and the first term on the right-hand side,

representing the redistribution of mass within the water column due to the mean time-averaged turbulent mass flux, yielding

$$\frac{\mathrm{d}}{\mathrm{d}t}\log\left(d(t)\right)c_0(y) = -\frac{\partial}{\partial y}\left(\frac{f(y,t)}{d(t)}\overline{\langle v'c_0'\rangle_\phi}^{T/2}\right) + \frac{1}{Re_{\delta_s}Sc}\frac{\mathrm{d}^2}{\mathrm{d}y^2}c_0(y). \tag{5.3}$$

The exact decay law for $d(t)$ can now be extracted, regardless of the functional form of $f(y,t)$, by integrating (5.3) in the wall-normal direction, yielding

$$\frac{\mathrm{d}}{\mathrm{d}t}\log\left(d(t)\right) = -\frac{1}{Re_{\delta_s}ScC_{0,B}}\frac{\mathrm{d}}{\mathrm{d}y}c_0(y)\bigg|_{y=0}, \tag{5.4}$$

where $C_{0,B}$ is the integral between 0 and $L_y$ of $c_0(y)$. By introducing the mean rate of decay

$$k = \frac{1}{C_{0,B}}J_{0,swi}, \tag{5.5}$$

where

$$J_{0,swi} = \left(Re_{\delta_s}Sc\right)^{-1}\frac{\mathrm{d}}{\mathrm{d}y}c_0(y)\bigg|_{y=0}, \tag{5.6}$$

the final expression for $d(t)$ (or $c_\infty(t)$) becomes

$$c_\infty(t) = d(t) = d_0\mathrm{e}^{-kt}, \tag{5.7}$$

where $d_0$ is the normalized free-stream value of the monotonically decaying component of oxygen concentration at $t = 0$, intended here as the virtual origin of the self-similarly decaying concentration field. The relations (5.5) and (5.6) are an important analytical constraint between $c_\infty(t)$ and $c_0(y)$, confirming the interpretation of $c_0(y)$ as the self-similar steady component of the mean oxygen distribution, responsible for the mean bulk concentration rate of decay (with time constant $k^{-1}$), and of (5.6) as the corresponding flux across the SWI. The constraint between $d(t)$ and $c_0(y)$ in (5.5) is a direct consequence of the self-similar functional form (4.3) and does not allow an independent evaluation of these two quantities. An iterative procedure is therefore necessary to determine $d(t)$ and $c_0(y)$ from the transient data and is described in appendix A.

Given the very slow decay rate ($k \ll T^{-1}$), due to the limiting effects on the overall mass transfer rate of the high-Schmidt-number scalar, a Taylor expansion of (5.7) about $t = 0$, truncated to first-order,

$$d(t) = d_0\mathrm{e}^{-kt} \simeq d_0(1 - kt), \tag{5.8}$$

provides a very accurate approximation for $d(t)$ especially in the early stages of decay. This explains the successful adoption of the linear fitting in the preliminary analysis carried out in § 4, to estimate $d(t)$. At this stage, due to the limited time span covered by the numerical results (with respect to the very long time scales of decay of the scalar field) it is not possible to appreciate in figures 2 and 3 the difference between a linear and an exponential decay of the time series. This issue will be addressed in § 7.

In the derivation above, a self-similar formulation such as (4.3) has led, via mathematical manipulation of the governing partial-differential equations, to the exact definition of the decay law (the scaling parameter for the solution in time), derived from the integration of an ordinary-differential equation (5.4); this is consistent with

a commonly accepted approach in the study of self-similarly decaying flows (Pope 2000).

Substituting (5.7) into (5.3) yields

$$-kc_0(y) = -\frac{\partial}{\partial y}\left(\left[\frac{f(y,t)\mathrm{e}^{kt}}{d_0}\right]\overline{\langle v'c_0'\rangle_\phi}^{T/2}\right) + \frac{1}{Re_{\delta_s}Sc}\frac{\mathrm{d}^2}{\mathrm{d}y^2}c_0(y). \tag{5.9}$$

It follows that the term in square brackets must be a constant function of time, and therefore, in general, only a function of $y$, say, $g(y)$, resulting in

$$f(y,t) = g(y)d_0\mathrm{e}^{-kt}. \tag{5.10}$$

At this point we can extract the budget for the oscillating component of the oxygen distribution by subtracting (5.3) from (5.1) and using (5.10), yielding

$$\begin{aligned}&\frac{1}{d(t)}\left(\frac{\partial}{\partial t}\widetilde{d}(y,t)\right)\widetilde{c}_0(y,\phi) + \frac{\widetilde{d}(y,t)}{d(t)}\frac{\partial}{\partial t}\widetilde{c}_0(y,\phi)\\ &\quad= -\frac{\partial}{\partial y}\left(g(y)\widetilde{\langle v'c_0'\rangle_\phi}\right) + \frac{1}{Re_{\delta_s}Sc}\frac{\mathrm{d}^2}{\mathrm{d}y^2}\left[\frac{\widetilde{d}(y,t)}{d(t)}\widetilde{c}_0(y,\phi)\right].\end{aligned} \tag{5.11}$$

The presence of a non-zero, periodic turbulent forcing term (first term on the right-hand side, only dependent on the phase angle $\phi$ for every $y$) implies that $\widetilde{d}(y,t)$ cannot be a constant function of time and, in particular, that at least one of the other terms in (5.11) must be periodic. This implies that

$$\frac{\widetilde{d}(y,t)}{d(t)} = h(y) \tag{5.12}$$

where $h(y)$ is some function of $y$, and, therefore,

$$\frac{1}{d(t)}\frac{\partial}{\partial t}\widetilde{d}(y,t) = l(y), \tag{5.13}$$

where $l(y) = -kh(y)$. It can be shown that if the ratio in (5.12) changes with time $t$, a logical contradiction is reached. The function $h(y)$ can be, in this case, arbitrary since the only assumption made when defining $\widetilde{d}(y,t)$ is that $\widetilde{c}_0(y,\phi)$ must be periodic in time, consistently with the rationale behind the formulation of (4.8). It is has been shown that this condition is already satisfied by (5.12), regardless of the functional form of $h(y)$. For the sake of simplicity we will, therefore, take $h(y) = 1$.

The last unknown function left to determine is $g(y)$ in (5.10), which is a natural consequence of the assumptions made when defining $f(y,t)$ in (4.12). The result in (5.10) states that the decay rate of the amplitude of the fluctuating field scales, in time, with the same law as the steady and oscillating component. This can be heuristically explained by noticing that production of the variance of $C'(\boldsymbol{x},t)$ must decay as $d(t)^2$, since it is proportional to the product of the ensemble-average scalar gradient and the turbulent flux, both decaying as $d(t)$. Some insight on the role of $g(y)$ can be gained from the scalar variance budget of the statistically steady self-similar stochastic component $c_0'(\boldsymbol{x},t)$, which reads

$$\begin{aligned}&-k\,g(y)\langle c_0'(\boldsymbol{x},t)^2\rangle_\phi + g(y)\frac{\partial}{\partial t}\frac{1}{2}\langle c_0'(\boldsymbol{x},t)^2\rangle_\phi\\ &\quad= -\overline{\langle c_0'v'\rangle_\phi}^{T/2}\frac{\mathrm{d}}{\mathrm{d}y}c_0(y) - \widetilde{\langle c_0'v'\rangle_\phi}\frac{\mathrm{d}}{\mathrm{d}y}c_0(y)\end{aligned}$$

$$-\overline{\langle c_0' v' \rangle_\phi}^{T/2} \frac{\partial}{\partial y} \widetilde{c}_0(y,\phi) - \widetilde{\langle c_0' v' \rangle_\phi} \frac{\partial}{\partial y} \widetilde{c}_0(y,\phi)$$

$$- \left\langle c_0' \frac{\partial}{\partial x_j} \left( u_j' g(y) c_0' \right) \right\rangle_\phi + \frac{1}{Re_{\delta_s} Sc} \left\langle c_0' \nabla^2 (g(y) c_0'(\boldsymbol{x}, t)) \right\rangle_\phi, \tag{5.14}$$

revealing that the (four) production terms are unaffected by the choice of $g(y)$. The latter, therefore, simply determines a redistribution of the variance in $y$ among the turbulent diffusion and dissipation terms (and, accordingly, the accumulation terms on the left-hand side), with no physical relevance. Therefore, analogously to $h(y)$, we will pose $g(y) = 1$.

## 6. Scalar variance budgets and regenerative cycle

We intend to derive here the scalar variance budgets relative to the mean fields $c_0(y)$ and $\widetilde{c}_0(y,\phi)$. The goal is to show how the linearity of the governing equations for the passive scalar field allows for the overlap between a complete steady and a periodic turbulent mass transfer problem, both forced by the same underlying velocity field.

The final functional form of the decomposition (4.14) is

$$c(\boldsymbol{x}, t) = \left[ c_0(y) + \widetilde{c}_0(y,\phi) + c_0'(\boldsymbol{x}, t) \right] c_\infty(t). \tag{6.1}$$

The budget for the steady component, $c_0(y)$, is

$$-k c_0(y) = \frac{\mathrm{d}}{\mathrm{d}y} \left[ J_0(y) - \overline{\langle v' c_0' \rangle_\phi}^{T/2} \right], \tag{6.2}$$

where

$$J_0(y) = \frac{1}{Re_{\delta_s} Sc} \frac{\mathrm{d}}{\mathrm{d}y} c_0(y). \tag{6.3}$$

Equation (6.2) highlights how the non-zero divergence of the total steady component of the mass flux (right-hand side), is balanced by the constant mean decay rate (on the left-hand side), originating from the scalar accumulation term in (2.3). In the limit $k \to 0$, (6.2) takes on the form of a balance between molecular and turbulent mass flux, typical of equilibrium mass-transfer problems. This is also true for the cycle-average component of the budget (5.14), which reads

$$-k \overline{\langle c_0'(\boldsymbol{x}, t)^2 \rangle_\phi}^{T/2} = -\overline{\langle c_0' v' \rangle_\phi}^{T/2} \frac{\mathrm{d}}{\mathrm{d}y} c_0(y) - \frac{\partial}{\partial x_j} \overline{\left\langle u_j' \frac{1}{2} {c_0'}^2 \right\rangle_\phi}^{T/2}$$

$$+ \frac{1}{Re_{\delta_s} Sc} \overline{\left\langle c_0' \nabla^2 c_0'(\boldsymbol{x}, t) \right\rangle_\phi}^{T/2}, \tag{6.4}$$

where steady production, turbulent and molecular diffusion and dissipation terms are clearly distinguishable and balance each other in the limit $k \to 0$. The relations (6.4) and (6.2) describe the typical budget for a mean and a fluctuating scalar field found in statistically steady mass-transfer problems. No traces of the periodic forcing provided by the oscillating turbulent velocity field are present. This idea is illustrated in figure 6 where cycle $S$ represents the steady scalar variance budget (6.4). The latter is sustained by part of the fluctuating velocity field that contributes to the cycle-average mass flux, which sustains the mean gradients of $c_0(y)$ responsible, in turn, for the scalar variance production (hence, closing the cycle). These are effectively mixing dynamics observed in a steady-state turbulent mass-transfer problem (see discussion on this point

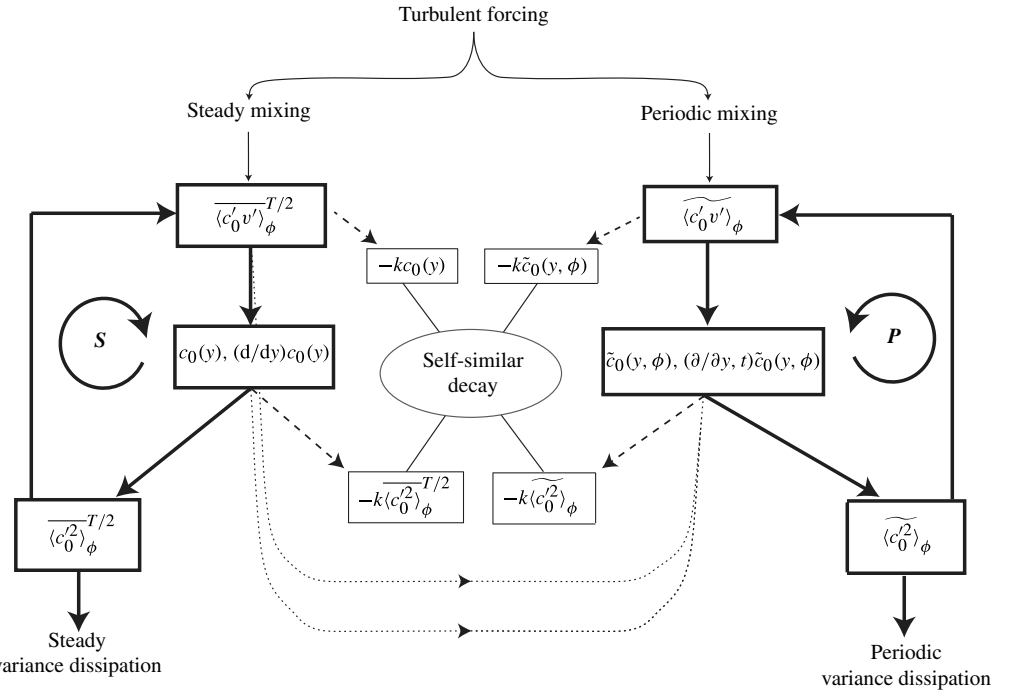


FIGURE 6. Illustration of the steady *(S)* and periodic *(P)* concentration and variance cycles exhibiting quasi-equilibrium characteristics, representing budgets (6.2) and (6.4), and (6.5) and (6.7), respectively. The energy input to these cycles is provided by the steady and the periodic component of the turbulent mixing induced by the oscillatory flow. Thick arrows indicate the direction of scalar variance transfer within the two cycles. In *S* the steady component of the turbulent mass flux, $\overline{\langle c_0' v' \rangle_\phi}^{T/2}$, sustains the non-oscillating component of the mean scalar field, $c_0(y)$, via (6.2), which sustains the production of the steady component of the scalar variance $\overline{\langle c'_0{}^2 \rangle_\phi}^{T/2}$, via (6.4), which sustains the scalar fluctuations needed to generate the turbulent mass flux, therefore closing the cycle. Analogous equilibrium-like dynamics are present in the periodic cycle *(P)*. The dashed lines with arrows indicate the loss of scalar concentration and scalar variance balanced by the self-similar decay (i.e. the first terms on the left-hand side of (6.2), (6.4), (6.5) and (6.7)). Dotted lines with arrows indicate the presence of an interaction between the two cycles: the steady component of the turbulent mass flux and the non-oscillating component of the mean scalar gradient also sustain the production of the oscillating component of the scalar variance (6.7).

in §§ 7 and 8). The non-zero accumulation terms (multiplied by $-k$) balance the right-hand sides of (6.4) and (6.2). In other words, the non-zero flux divergence sustains the self-similar decay, as illustrated by the dashed lines in figure 6.

Analogous considerations can be made for the oscillating component $\tilde{c}_0(y,\phi)$ for which the conservation equation is readily derived

$$-k\tilde{c}_0(y,\phi) + \frac{\partial}{\partial t}\tilde{c}_0(y,\phi) = \frac{\partial}{\partial y}\left[\tilde{J}_0(y,\phi) - \widetilde{\langle c_0' v' \rangle_\phi}\right], \tag{6.5}$$

where

$$\tilde{J}_0(y,\phi) = \frac{1}{Re_{\delta_s} Sc}\frac{\partial}{\partial y}\tilde{c}_0(y,\phi). \tag{6.6}$$

The corresponding variance budget equation, obtained by removing the cycle-averaged component from (5.14), reads

$$-k\widetilde{\langle c_0'^2\rangle}_\phi + \frac{\partial}{\partial t}\frac{1}{2}\widetilde{\langle c_0'^2\rangle}_\phi = -\widetilde{\langle c_0'v'\rangle}_\phi \frac{\partial}{\partial y}\left[c_0(y) + \widetilde{c}_0(y,\phi)\right] - \overline{\langle c_0'v'\rangle}_\phi^{T/2}\frac{\partial}{\partial y}\widetilde{c}_0(y,\phi)$$
$$- \frac{\partial}{\partial x_j}\left\langle \widetilde{u_j'\frac{1}{2}c_0'^2}\right\rangle_\phi + \frac{1}{Re_{\delta_s}Sc}\widetilde{\langle c_0'\nabla^2 c_0'\rangle}_\phi. \tag{6.7}$$

In the limit $k \to 0$, the set of equations (6.7) and (6.5) describes a statistically periodic turbulent scalar field in dynamical equilibrium. There are two sources sustaining this periodic scalar variance cycle, illustrated as cycle $P$ in figure 6: the oscillating and the steady cycle-average component of the turbulent mass flux working, respectively, against the total and the oscillating component of the mean scalar gradient (first and second term on the right-hand side of (6.7)). This can be interpreted as a mass-transfer problem in a turbulent oscillating boundary layer with an imposed alternating zero-mean flux at the wall, $\widetilde{J}_{0,swi}$ (shown later in figure 14).

Mathematically, the periodic component of the concentration field satisfies a set of ordinary-differential equations (one for every $y$), each describing a linear system subject to a zero-mean harmonic forcing. The latter is physically due to the statistically periodic evolution of the turbulent coherent structures modulating the instantaneous scalar field (discussed in § 8).

## 7. Computational domain and Schmidt number effects

The transient data shown so far have been generated on a large computational domain to improve the convergence of the flow statistics (shown later). This has, however, only allowed simulation of a short time span, relative to the characteristic time scale of decay, $k^{-1}$. Further evidence corroborating the assumptions and analytical predictions made so far could not be gathered. These include the exponential nature of the decay of the ensemble-average concentration field, the assumptions regarding the nature of the stochastic component (4.12) and the equilibrium arguments made in the analysis of the scalar variance cycles (§ 6). It is also important to assess whether the self-similar form (6.1) is valid for lower Schmidt numbers and different domain sizes. Neither of the two restrictions, however, has been explicitly introduced in the mathematical derivations made so far.

To address these questions we first performed another simulation with the same resolution but a smaller domain size (only in the spanwise and streamwise directions, resulting in $L_x = 25$, $L_y = 13\pi$, $L_z = 15$), inspired by the minimal channel simulations of Costamagna *et al.* (2003). This has allowed emphasis on the signature of the stochastic component (4.12) in the plane-averaged signals and the obtaining of much longer time series, while still retaining the essential features of turbulent transport (Jiménez & Moin 1991). Such a small domain does not allow a natural evolution of the turbulent structures; however, from a purely statistical point of view, the results obtained from such numerical experiments are equally valid, being still a turbulent solution of the governing equations of the flow. The arguments leading to (6.1) have been, in fact, for the most part statistical and analytical.

Results in figure 7 reveal the same self-similar structure as in (4.3). The time series exhibit a more intermittent behaviour than in figure 3, dominated by low-frequency, ramp–cliff-like variations (with sudden aperiodic drops and/or peaks in the

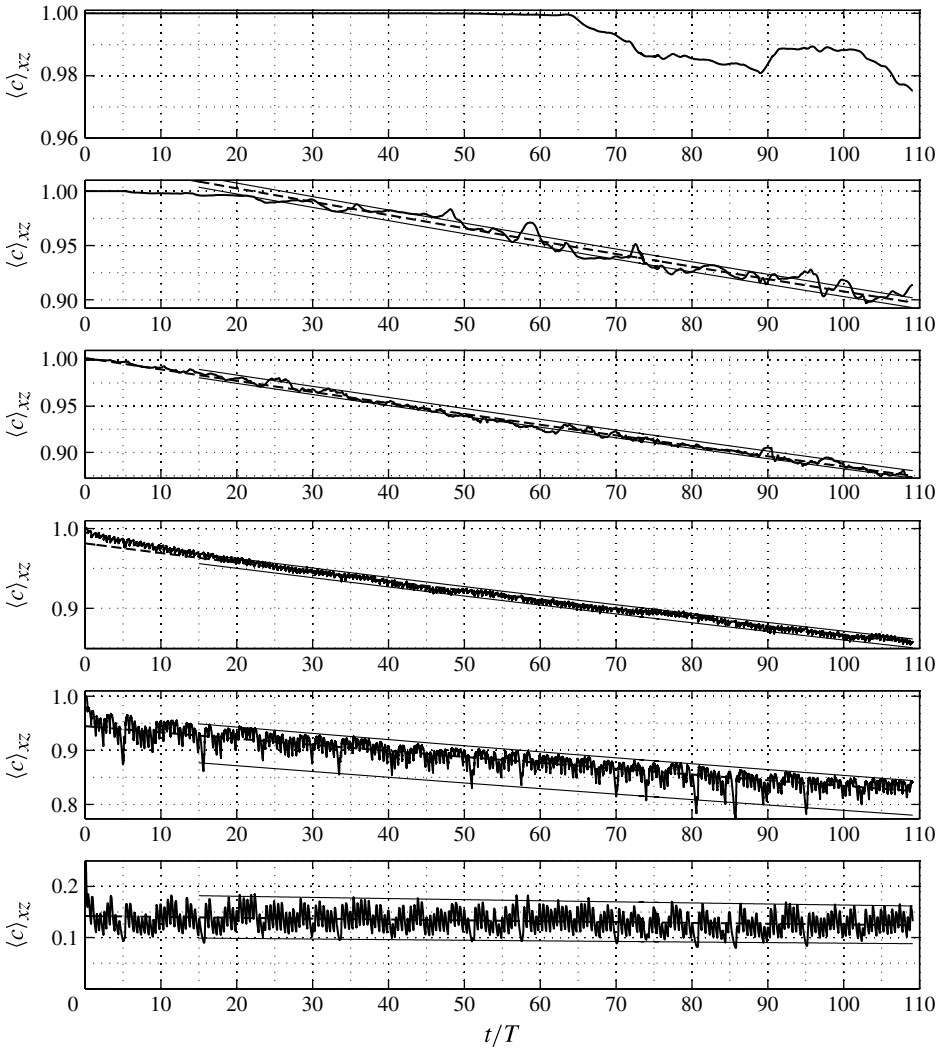


FIGURE 7. Time series of plane-averaged oxygen concentrations (from top to bottom) at $y = 40, 35, 25, 0.5, 0.1, 0$ for $\chi^* = 700\,\mathrm{mg\,l^{-1}}$ for minimal-channel calculations. Signal is bounded on both sides by an exponentially decaying envelope (——) with the same rate of decay as the exponential fit used for the monotonically decaying component (– – –), analogously to figure 3.

concentration value) with a characteristic period of the order of $5T$. This confirms their non-coherent, stochastic nature.

The most striking difference occurs in the evolution of the top-boundary concentration where the beginning of the turbulent entrainment occurs only after approximately 50 cycles. This is most likely due to the small computational domain, which limits the size of the larger structures governing the entrainment in the outer region. In the previous simulation, entrainment of the top-boundary concentration value occurs almost immediately after $t = 1.5T$ (figure 3). This suggests that the self-similar decay is first established in the fully mixed region (approximately $y < 20$)

and then gradually extends into the outer region at a rate depending on the size of the resolved turbulent structures. It appears that the entrainment front (i.e. the one locally setting the start of the self-similar decay) could spread indefinitely in the wall-normal direction. That is to say, after a sufficiently long time, any $y$ can be chosen as a reference 'top boundary' to evaluate the scaling function $d(t)$ or $c_\infty(t)$. Previous numerical trials have shown that the onset of the self-similar decay in the non-fully mixed region is rather sensitive to initial conditions and grid resolution. The purely intermittent nature of mixing in this region requires *ad-hoc* numerical and experimental investigations which are outside the scope of the present study.

While entrainment in the outer region is inhibited by the small domain size, mixing in the near-wall region is enhanced, resulting in a more rapid decay rate with respect to the larger domain size case (direct comparison not shown). We speculate that this is due to turbulent bursting events being forced to occur more frequently, spuriously enhancing the mass transfer, as a result of the confinement of near-wall structures (Jiménez & Moin 1991). The overall decay rate of a passively advected scalar can be an alternative indicator of an appropriate domain size rather than two-point correlations, for a simulation of this sort, given the strong spanwise coherence introduced by Kelvin–Helmholtz-like rollers (Hino *et al.* 1983) in this regime.

The results shown so far have demonstrated that the domain size does not alter the structure of the self-similar decay, but only the decay rate. The extended time span covered by the data shown in figure 7 still does not allow us to verify whether the decay is actually exponential and whether it involves all the components of the solution, as suggested by (6.1). Lower Schmidt numbers accelerate the rate of decay and allow us to verify the predicted exponential decay rate. To address these points, we have carried out other minimal-channel simulations with no sediment layer but on the same computational grid for the water side with homogeneous Dirichlet and Neumann boundary conditions for the scalar field, at the bottom wall and the top boundary, respectively, for Schmidt numbers $Sc = 0.1, 1, 10, 100$ and 1000. The same self-similar structure of decay is observed in all cases (figure 8). The corresponding profiles of $c_0(y)$ (not shown) exhibit the same shape as in figure 4 but reaching zero at the wall, consistently with the imposed boundary conditions. Most importantly, the rapid decay present in the lower-Schmidt-number cases allows one to appreciate the exponential decay of both the non-oscillating and oscillating components of the ensemble-average field. This supports the analytical predictions made in § 5, where no explicit assumption on the magnitude of the Schmidt number has been made.

Reducing the Schmidt number also decreases the coherence of the oscillating component, which is driven by advective transport mechanisms (6.5), contaminating it with molecular diffusion effects. As expected, irregularities such as the ramp–cliff structures are damped at lower Schmidt numbers. Experimental investigations spanning a similar range of Schmidt/Prandtl numbers would allow us to assess whether numerical simulations not resolving sub-Kolmogorov scales correctly reproduce the observed large-scale intermittency effects and if *ad-hoc* subgrid-scale modelling is required.

The predominant effect of the Schmidt number is to regulate the overall mean decay rate, $k$ (figure 9). Its asymptotic trend in the high-Schmidt number-limit is suprisingly consistent with classic parameterizations of steady-state high-Schmidt-number turbulent mass transfer (Shaw & Hanratty 1977; Scalo *et al.* 2012*a*), and with the physical interpretation of $c_0(y)$ as the mean scalar profile of a statistically steady mass-transfer problem (as discussed in § 6). The very long time scales associated with slow decay rates (for $Sc \gg 1$) allow turbulent mixing (evolving over times scales

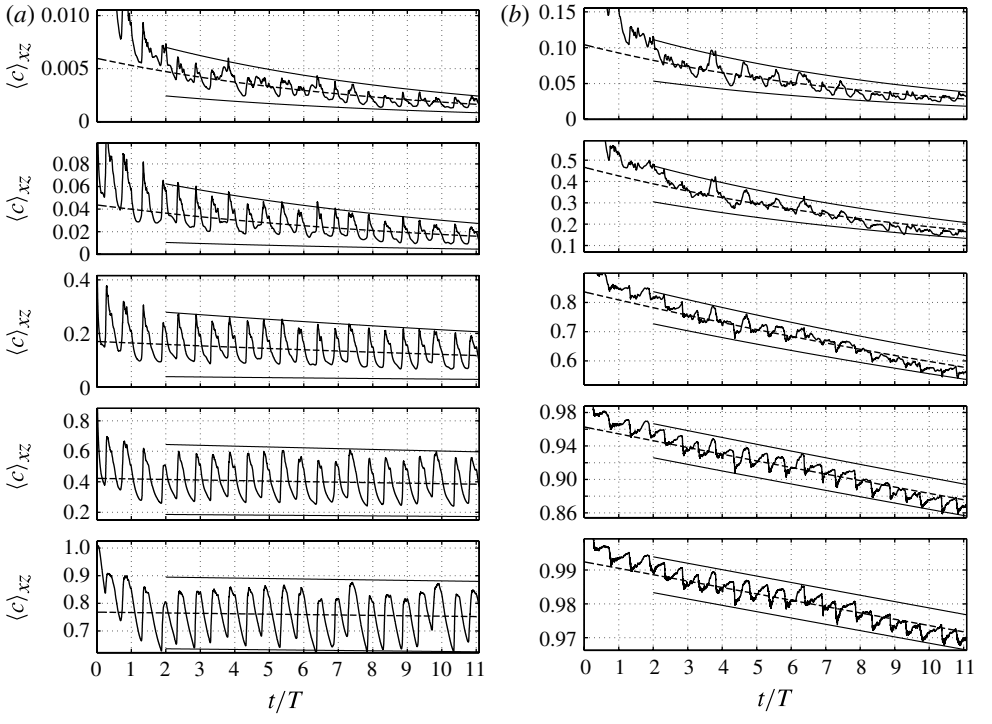


FIGURE 8. Time series of a plane-averaged decaying passive scalar at $y = 0.05$ (*a*) and $y = 10.3$ (*b*) for (from top to bottom) $Sc = 0.1,\ 1,\ 10,\ 100,\ 1000$ for minimal-channel calculations with no sediment layer. Signal is bounded on both sides by an exponentially decaying envelope (——) with the same rate of decay as the exponential fit used for the monotonically decaying component (– – –).

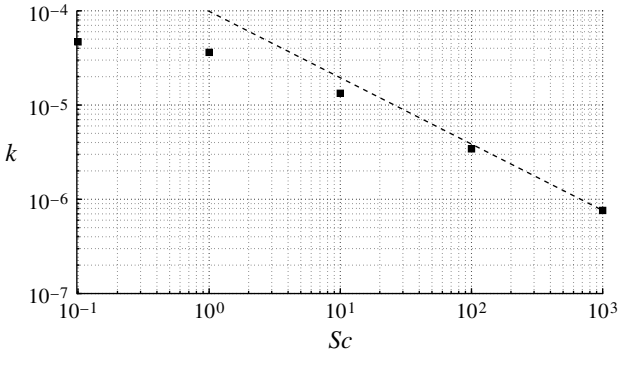


FIGURE 9. Decay constant $k$ as a function of Schmidt number for minimal-channel oscillating boundary layer calculations with no sediment layer. Asymptotic behaviour $\propto Sc^{0.704}$ as suggested by the high-Schmidt-number mass-transfer parameterization by Shaw & Hanratty (1977) (– – –).

of the order of $T$) to be, within very good approximation, in equilibrium with the background concentration value, creating quasi-statistically steady (and statistically

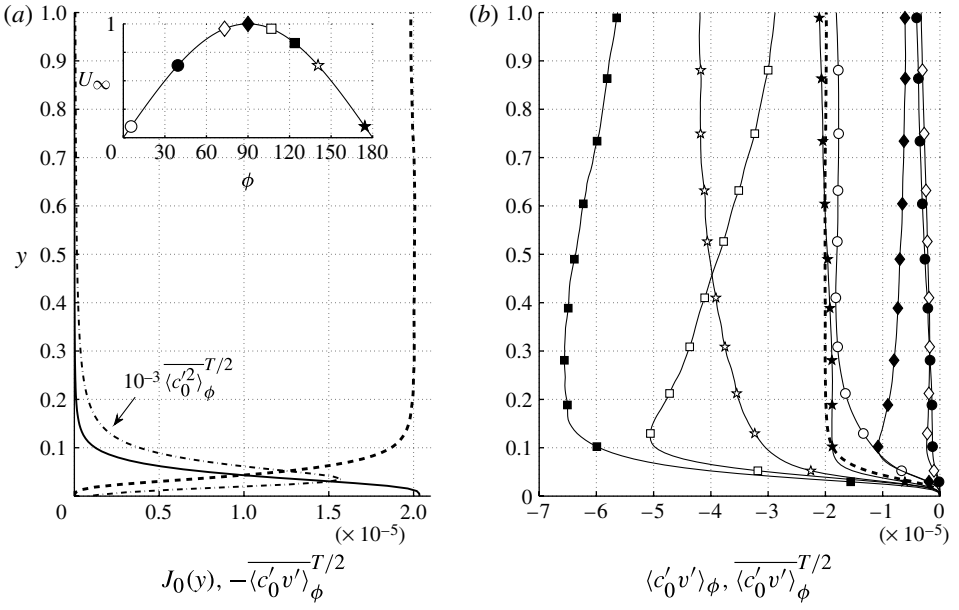


FIGURE 10. Near-wall region statistics. (*a*) Cycle-averaged mass flux $\overline{\langle c_0' v'\rangle_\phi}^{T/2}$, (– – –), scalar variance, $\overline{\langle c_0'^2\rangle_\phi}^{T/2}$ (–·–), and steady component of the diffusive flux, $J_0(y)$ (——). (*b*) Profiles of total and cycle-averaged turbulent mass flux, $\langle c_0' v'\rangle_\phi$ and $\overline{\langle c_0' v'\rangle_\phi}^{T/2}$, respectively, for different phases shown in the inset in (*a*).

periodic) conditions for the mass transfer as illustrated in figure 6. This condition is exactly satisfied in the limit $k \to 0$. This suggests that in cases where the decay occurs over time scales comparable to the oscillation period, there might not be a truly statistically periodic fluctuating component in the scalar field, therefore violating the assumption that $f(y, t)$ in (4.12) is a non-stochastic quantity. Experimental and/or numerical investigations at various Schmidt/Prandtl numbers would have to be carried out, comparing directly the statistical distributions of the fluctuating field at one phase (derived via careful ensemble averaging) with a phase-averaged distribution generated via the decomposition (6.1) from the same case.

## 8. Mass transport dynamics

The possibility of extracting a steady, $c_0(y)$, and a periodic, $\widetilde{c}_0(y, \phi)$, field and their scalar-variance budgets (appendix B), (6.4) and (6.5), from the decaying scalar allows us to investigate the transport dynamics relying on a statistical description of the flow.

### 8.1. *Monotonic self-similarly decaying concentration field*

The scalar field satisfying the mass-transfer problem (6.2) and (6.4) exhibits all the traits of steady high-Schmidt-number mass transfer to a solid wall (Pinczewski & Sideman 1974; Scalo *et al.* 2012*a*). Figure 10 shows the very rapid transition across the diffusive sublayer from molecular to turbulent transport, occurring in approximately 0.2 Stokes thicknesses from the wall (at this Reynolds number). In particular, the profiles of the molecular and time-averaged turbulent fluxes (figure 11*a*)

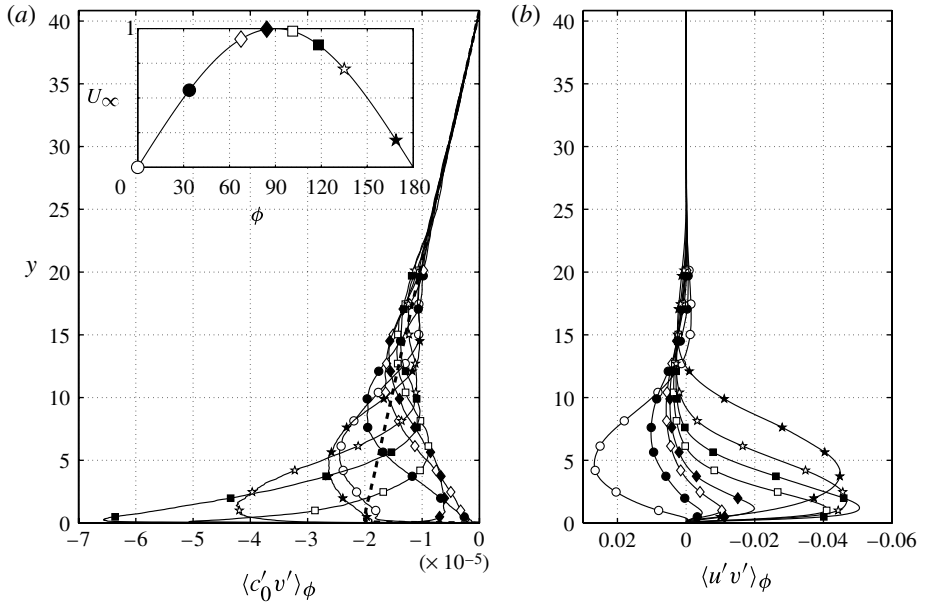


FIGURE 11. Profiles of turbulent-mass flux $\langle c_0' v' \rangle_\phi$ (*a*) and momentum flux $\langle u' v' \rangle_\phi$ (*b*) for semi-cycle $\phi = 0$–$180°$. Corresponding phases shown in the inset in (*a*). Also shown is the semi-cycle-averaged mass flux $\overline{\langle c_0' v' \rangle}^{T/2}$ (– – –).

decrease linearly with $y$ as the mean profile $c_0(y)$ approaches unity (figure 4), and the scalar variance peaks at approximately the inflection point of $J_0(y)$ (also observed in analogous steady mass transfer problems (Scalo *et al.* 2012*b*)).

While the Reynolds shear stresses, in the case of an oscillating boundary layer, are confined in a region close to the wall, $y < 25$ (figure 11*b*), the steady component of the turbulent mass flux, extracted in the self-similar decay range $t > 6T$, spans the entire resolved water column, consistent with equilibrium conditions of an open channel flow. This supports the considerations made in §§ 6 and 7, where it is argued that the existence of the self-similarity decay coincides with the establishment of a dynamical equilibrium in the scalar concentration and variance cycle.

### 8.2. *Periodic self-similarly decaying concentration field*

The periodic component of the scalar field satisfying the constraints (6.5) and (6.7) is driven by the oscillating component of the turbulent scalar flux, $\widetilde{\langle c_0' v' \rangle}_\phi$. The latter is only appreciable up to $y = 25$, after which the turbulent scalar mixing tends towards a statistical steady state, where all phase-averaged profiles collapse onto the time-averaged value. This suggests that the oscillating component of the oxygen field should vanish for $y > 25$.

The turbulent scalar flux is generated in the near-wall region, at the edge of the diffusive sublayer (figure 10*b*), where it exhibits the greatest variability (over more than one order of magnitude). A peak starts to appear towards the end of the acceleration phase, between $\phi = 70°$ and $\phi = 90°$, and rapidly grows in intensity until $\phi = 120°$, persisting at (approximately) a constant distance from the wall. It then propagates into the outer region while diffusing and decaying for most of the deceleration phase and the first part of the acceleration phase (figure 11*a*). The

signature of the periodic forcing is evident in the cyclic evolution of the mixing front for the scalar field, which however differs significantly from that of the momentum field.

While the evolution of the turbulent mass flux in the outer region appears to follow the Reynolds shear stress, its production phase, from $\phi = 70°$ to $\phi = 120°$ (figure 10*b*) is significantly shorter than that of the Reynolds shear stress (figure 11*b*), from $\phi = 40°$ to $\phi = 120°$ (figure 12). The gradual growth of the near-wall Reynolds shear stress peak triggers the build-up of the peak in turbulent mass flux, starting between $\phi = 70°$ and $\phi = 90°$. Both quantities start to propagate upwards around $\phi = 120°$, following the well-established coherent structure dynamics in the IT regime (Costamagna *et al.* 2003). However, the peak in the oscillating component of the turbulent mass flux loses phase coherence sooner (for $y > 9$) than the Reynolds shear stresses, while propagating upwards more rapidly. The turbulent mass flux modulates the concentration field distribution by entraining fluid layers richer in oxygen, less intensely for increasing distance from the wall.

The propagation speed of below- ($\widetilde{c}_0(y, \phi) < 0$) and above-average ($\widetilde{c}_0(y, \phi) > 0$) concentration layers is determined by the aforementioned evolution pattern of the oscillating mixing front (figure 13*a*). The amplitude of the oscillating component rapidly decreases (figure 13*b*) as the amplitude of the oscillating turbulent mass flux also decays with $y$. Layers of above-average concentration at a certain $y$ only appear after a peak in turbulent mass flux has occurred at the same $y$ approximately 90° earlier. The persistence of a growing peak in the turbulent mass flux from $\phi = 90°$ to $\phi = 120°$ creates a long-lasting above-average concentration layer very close to the wall, from $\phi = 135°$ to $\phi = 180°$. When the mixing front propagates outwards it loses intensity and it progressively leaves shorter-lasting above-average concentration layers. The signature of the periodic forcing in $\widetilde{c}_0(y, t)$ disappears almost completely after $y > 14$. In this region, the transport is characterized by a statistically steady intermittent entrainment of high-in-oxygen fluid, as anticipated in § 4.2.

The mathematical relationship in (6.5) confirms the dynamics observed in figure 13. The oscillating component of the turbulent mass flux is the forcing term in (6.5) for the periodic component of the scalar field and the ratio between their Fourier transforms is given by the transfer function

$$G(\omega) = \frac{1}{j\omega - k}. \tag{8.1}$$

The base angular frequency is $\omega T/2 = 1$ and the slow decay rate determines, in our case, $kT/2 = 1 \times 10^{-4}$ and $6 \times 10^{-4}$ for, respectively, the low- and high-absorption cases. This means that the transfer function can be approximated by $G(\omega) \simeq 1/j\omega$, confirming that $\widetilde{c}_0(y, \phi)$ is delayed by ∼90° with respect to the forcing turbulent mass flux as shown in figure 13.

### 8.3. *Momentum and mass transfer at the wall*

The main interest of the geophysical community is to predict the mass-transfer rate of solutes across the SWI relying on outer-layer flow parameters. Typically, a value for the friction velocity is estimated from the free-stream current intensity and used to infer the near-wall levels of turbulent mixing and predict the mass flux at the interface, assuming equilibrium conditions (Boudreau & Jørgensen 2001). The very low diffusivity of a high-Schmidt-number passive scalar, however, results in long adaptation times of the diffusive sublayer to the turbulent forcing, even for high-

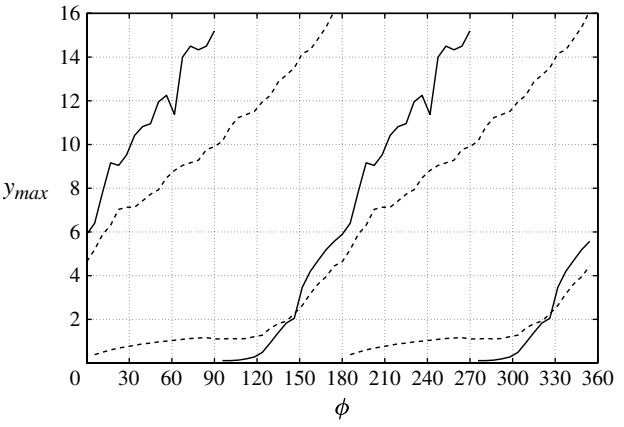


FIGURE 12. Location of negative peak in the oscillating turbulent mass flux $\widetilde{\langle c_0' v' \rangle}_\phi$ (——), and of negative and positive peak in Reynolds shear stress, $\langle u' v' \rangle_\phi$ (– – –), as a function of the phase angle $\phi$.

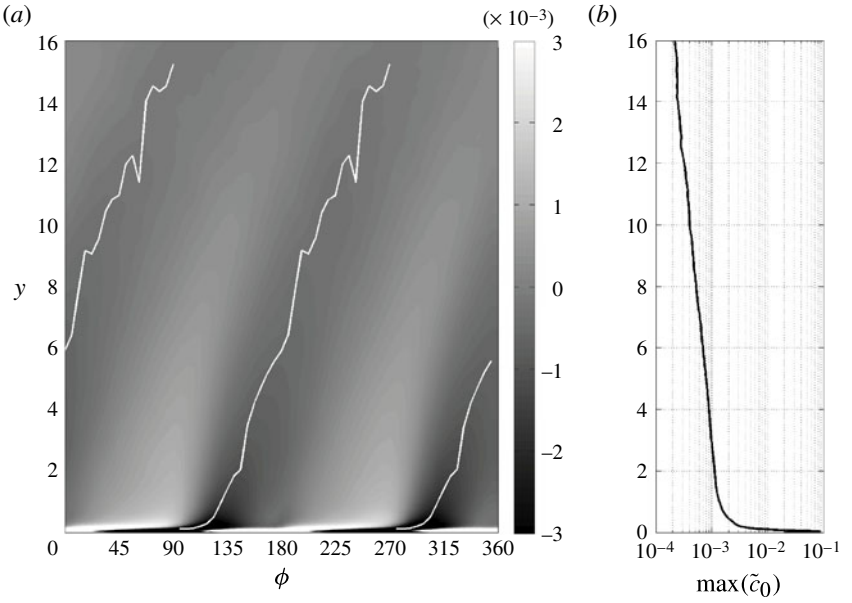


FIGURE 13. (*a*) Contour map of the oscillating component $\widetilde{c}_0(y, \phi)$ with the location of the negative peak in the oscillating turbulent mass flux (——); and (*b*) profile of the corresponding peak value.

Reynolds-number flows, with important consequences on low-order modelling of the flux (Scalo *et al.* 2013).

The non-equilibrium state of turbulence in the low-Reynolds-number oscillating boundary layer analysed in the present work emphasizes the aforementioned delay in the response of the diffusive sublayer. This is shown by the response of the periodic

component of the molecular mass flux at the SWI,

$$\widetilde{J}_{0,swi}(\phi) = \left(Re_{\delta_s} Sc\right)^{-1} \frac{\partial}{\partial y} \widetilde{c}_0(y, \phi)\Big|_{y=0}, \tag{8.2}$$

to changes in the viscous-sublayer thickness, represented by the phase-averaged wall-shear stress $\tau_w(\phi)$ (figure 14). The wall-shear stress exhibits an extended plateau from $\phi = 45°$ to $\phi = 120°$ corresponding to the residence time of the Reynolds shear-stress peak at $y \simeq 1$ (figure 12). The peak in $\widetilde{J}_{0,swi}(\phi)$ occurs after $\phi = 135°$, delayed with respect to the wall-shear stress and the turbulent mass flux peak at $y = 0.2$. It actually occurs only when an above-average value of oxygen concentration ($\tilde{c}_0(y, \phi) > 0$) is accumulated in the diffusive sublayer ($y < 0.2$), between $\phi = 135°$ and $\phi = 180°$ (figure 13).

The cascade of events leading to the periodic enhancement of the average diffusive mass flux at the wall are separated by time lags comparable to the oscillation period. The same dynamics are observed at the instantaneous level in statistically steady high-Schmidt-number turbulent mass-transfer problems (Scalo *et al.* 2012*a*). During a bursting event, energetic near-wall eddies reach the wall where they lose momentum, increasing the local value of the wall-shear stress. This is followed by an increase in the local value of scalar concentration and the scalar flux, occurring with a well-defined delay, comparable to a large-eddy turnover time.

Higher Reynolds numbers regularize the turbulent production cycle showing, already by $Re_{\delta_s} > 1800$, no significant phase difference between the main current and the wall-shear stress (Spalart & Baldwin 1989; Jensen *et al.* 1989). An attenuation of the variation throughout the oscillatory cycle of the turbulent production intensity is expected to reduce the amplitude of the oscillatory component of turbulent mass flux in the water column (figure 11*a*) and of the molecular mass flux at the wall (8.2), while the background steady component of the flux (6.3) becomes more significant. The phase lag between between the mass flux and wall-shear stress should also be significantly reduced in the fully turbulent regime ($Re_{\delta_s} > 1800$), which is expected to be primarily characterized by steady-state mass-transfer dynamics (§ 8.1) rather than oscillatory (§ 8.2).

A separate set of simulations of the velocity field only covering the range of $Re_{\delta_s} = 800$–$3600$ (not shown), reveals a growth in the boundary layer thickness (in $\delta_s^*$) for increasing $Re_{\delta_s}$. For a given kinematic viscosity, higher Stokes–Reynolds numbers can be achieved by increasing either the free-stream velocity $U_{om}^*$ or the oscillation period $T^*$. In the first case, near-wall turbulent mixing is energized by the enhanced kinetic energy coming from the large scales and upward turbulent diffusion of near-wall vorticity accelerated. In the second case, the longer persistence of the forcing allows for a longer expansion of the turbulent boundary layer via the same mechanisms. The diffusive-sublayer thickness $\delta_D$ is expected to scale, for higher Reynolds numbers, proportionally to the viscous-sublayer thickness $\delta_\nu$, based on commonly adopted scaling laws such as $\delta_D/\delta_\nu = Sc^{1/3}$. This is expected to directly affect the molecular mass transfer at the interface. However, Scalo *et al.* (2012*a*) have argued that, for increasing Reynolds number, a progressively smaller portion of the near-wall turbulent coherent structures modulate the mass transfer at the wall, suggesting an increasingly rapid thinning of $\delta_D$ with respect to $\delta_\nu$ for increasing Reynolds numbers. Accurate high-Schmidt-number mass-transfer simulations covering a wide range of Reynolds numbers from the IT to the FT regimes would have to be performed to confirm the predicted trends.

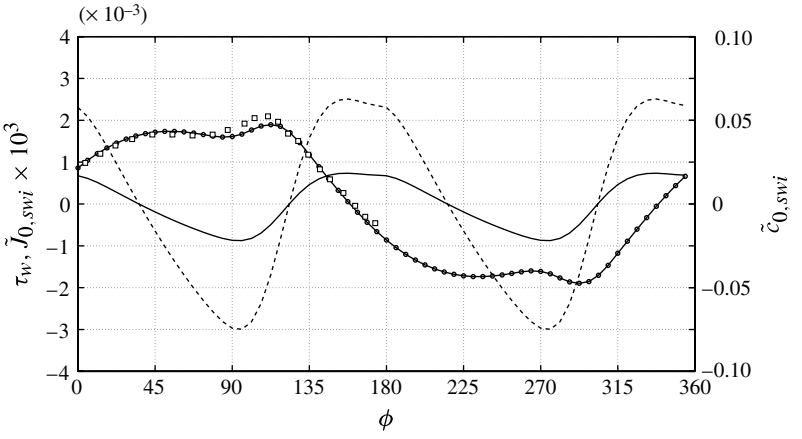


FIGURE 14. Phase-averaged wall-shear stress: present calculation (-•-); data from Jensen *et al.* (1989) (□); periodic component of the mass flux at the SWI, $\tilde{J}_{0,swi}$ (– – –); periodic component of the concentration $\tilde{c}_0$ at the SWI (——).

## 9. Conclusions

We have carried out DNS of the velocity field and LES of the scalar field to investigate the transient decay of dissolved-oxygen concentration due to sediment absorption in an oscillating boundary layer in the intermittently turbulent regime (IT). A Reynolds number of $Re_{\delta_s} = 800$ was chosen to maximize the asymmetry of turbulence between the acceleration and deceleration phases and investigate its effects on the sediment oxygen uptake. A uniform initial distribution of oxygen is left to decay with no re-aeration from the top boundary in a fully developed statistically periodic turbulent velocity field. The bulk oxygen concentration exhibits a very slow decay rate, with characteristic time scales very large compared to the oscillation period ($k^{-1} \gg T$), due to the limiting effect on the mass transfer of the very thin diffusive sublayer at the SWI.

Despite the highly intermittent state of the turbulent velocity field, after the first six cycles, the plane-averaged scalar field exhibits a surprisingly regular pattern of decay. A monotonically decaying component is identified on which coherent, zero-mean oscillations with a fundamental period of $T/2$ are superimposed. The former reveals a distinct self-similar structure, which, tested against the governing conservation equations for the scalar field, implies an exponential decay of the total ensemble- (or statistically) averaged scalar field. A linear decomposition of the instantaneous concentration field is then proposed, where self-similarity is extended to the fluctuating component, also shown to decay exponentially.

The identification of an analytical decay law has allowed a rescaling of the instantaneous scalar field in time, revealing the presence of two ergodic fields: a statistically steady and a periodic turbulent scalar field. Scalar variance budgets are derived for such fields, which resemble the well-known wall-bounded turbulence variance production, diffusion and dissipation cycle. This suggests a physical interpretation of the first field as a self-similarly decaying oxygen distribution in a statistically steady open channel flow; the second, as the solution of a turbulent mass transfer problem driven by oscillating boundary layer turbulence, with alternating flux at the wall and zero cycle-average bulk value.

Many of the assumptions made in the derivation of the solution decomposition and the analytical implications of the hypothesized self-similarity have been verified in a separate set of transient simulations performed on a smaller domain size (minimal-channel simulations), keeping the same boundary conditions, to achieve longer time series and, then, also for lower Schmidt numbers (without a sediment layer), to achieve a faster decay rate. The restricted domain size emphasizes the signature of the stochastic component of the passive scalar in the plane-averaged time series. In particular, the presence of ramp–cliff-like structures and low-frequency variations is made remarkably evident by the minimal-channel simulations, confirming their purely stochastic nature. A smaller domain size also limits the size of the larger turbulent structures, the ones governing the entrainment in the outer region, delaying the start of the self-similar decay at the top boundary. The speed at which the mixing front propagates in the outer region is reduced, while turbulent mixing of momentum remains confined in a well-defined region ($y < 25$ for $Re_{\delta_s} = 800$). The Schmidt number has been varied over four orders of magnitude showing that, in the high-Schmidt-number limit, the overall decay rate $k$, associated with the monotonically decaying component of the scalar field, scales like $Sc^{-0.704}$, surprisingly consistent with well-established empirical parameterizations for statistically steady high-Schmidt-number mass transfer. This confirms the physical interpretation of $c_0(y)$ as the solution of a steady-state mass-transfer problem. Simulations for lower Schmidt numbers confirm that both the non-oscillating and the oscillating components of the scalar field decay with the same exponential law, as analytically predicted.

An iterative procedure for the extraction of the ergodic component from the decaying scalar field was defined and has allowed us to investigate the turbulent mass transport mechanisms from a statistical point of view. It is shown that the oxygen distribution in the water column is modulated by the periodic upward propagation, during the deceleration phase, of highly mixed layers of fluid generated at the edge of the diffusive sublayer towards the end of the acceleration phase and growing in turbulent kinetic energy until the beginning of the deceleration phase. This turbulent flux production stage is linked to the well-known growth, instability and breakdown cycle of the near-wall streaks in oscillating boundary layers in the IT regime. The resulting highly mixed front propagates away from the SWI in the outer region, at approximately constant speed (slightly faster than the Reynolds shear stresses), in layers of low oxygen concentration. The periodic forcing modulates the concentration field in a shorter portion of the water column than the velocity field. Despite the highly intermittent state of turbulence, the oscillating component of the scalar field behaves like a linear harmonically forced system.

The persistence of high values of mass flux at the edge of the diffusive sublayer during the aforementioned turbulent flux production stage (at $y \sim 0.2$ between $\phi = 70°$ and $\phi = 120°$) is responsible for the accumulation of high concentration levels in the diffusive sublayer, occurring, on average, after $\Delta\phi = 90°$. The amplitude of the near-wall scalar oscillations exceeds by an order of magnitude that in the outer layer and is responsible for directly modulating the oscillating diffusive mass flux across the SWI. This is the signature of the highly non-equilibrium state of the turbulent mixing and is expected to become less significant for higher Reynolds numbers. The mixing dynamics analysed in the present work are also observed in the small-scale instantaneous turbulent transport processes that characterize statistically steady high-Schmidt-number mass transfer (Scalo *et al.* 2012*a*). We have shown that the different transport processes examined, which ultimately lead to the diffusive mass transfer across the SWI, occur statistically at specific times during the oscillating cycle;

analogous small-scale, instantaneous events occur, with the same pattern, during every quasi-periodic bursting cycle governed by near-wall coherent structures.

**Acknowledgements**

The authors acknowledge the financial support of the Natural Science and Engineering Research Council of Canada under the Discovery Grant Program and the Canada Research Chair program. The authors also thank the High Performance Computing Virtual Laboratory (HPCVL), Queen's University site, for the computational support. The authors also gratefully acknowledge the fruitful discussions with Professor M. Stastna, regarding, in particular, the present manuscript and, also, covering many other aspects of the general problem of oxygen depletion in water bodies.

## Appendix A. Decay rate, $k$, and self-similar profile $c_0(y)$ iterative calculation

The constraint in (5.5) is a direct consequence of the self-similar functional form (4.3) and leads to an iterative strategy to determine $d(t)$ and $c_0(y)$. A first guess for the constants $d_0$ and $k$ in (5.7) is obtained by performing a least-square fit of the plane-averaged scalar at the top boundary. The following iterative procedure is then carried out until convergence is reached on (5.5).

($a$) The current estimates for $k^{(i)}$ and $d_0^{(i)}$ ($i$th tentative form for $d(t)$) allow calculation of $c_0^{(i)}(y)$ ($i$th guess for the $c_0(y)$ profile) by fitting (4.3) with $d(t)$ from (5.7) to $\langle c(\boldsymbol{x}, t)\rangle_{xz}$, over an integer number of semi-periods at all $y$ locations.

($b$) The newly calculated $c_0^{(i)}(y)$ allows updating of $k^{(i)}$ to $k^{(i+1)}$ via (5.5).

($c$) The new guess for $k$ allows updating of $d_0^{(i)}$ to $d_0^{(i+1)}$ by the fitting $\langle c(\boldsymbol{x}, t)\rangle_{xz}$ at the top boundary for $k$ fixed to $k^{(i+1)}$.

($d$) If the condition (5.5) is not satisfied within the desired accuracy the procedure can be restarted from ($a$).

The iterative procedure converges to machine precision after four steps. The first error is of the order of 10 % and is reduced with longer time series. Note that the mean decay rate $d(t)$, determined with this procedure, is not influenced by $\widetilde{d}(y, t)$ or $f(y, t)$.

## Appendix B. Extraction of phase-averaged statistics from one-time plane-averaged data

The extraction of the three components in (6.1) requires an iterative procedure since $c_\infty(t)$ and $c_0(y)$ are interdependent via (5.5). Once $c_\infty(t)$ and $c_0(y)$ are determined, the instantaneous data, $c(\boldsymbol{x}, t)$, could be reprocessed as

$$\widetilde{c}_0(y, \phi) + c_0'(\boldsymbol{x}, t) = \frac{c(\boldsymbol{x}, t)}{c_\infty(t)} - c_0(y) \tag{B 1}$$

and, by means of phase averaging, any statistic could be evaluated. However, this would require loading the instantaneous data twice: once to calculate the time series of plane-averaged quantities, used to calculate $c_\infty(t)$ and $c_0(y)$; and, a second time, to reprocess the data via (B 1). Fortunately, the decomposition (6.1) can also be exploited to evaluate statistics directly from the plane-averaged quantities of the instantaneous transient data, without the need to reprocess the whole dataset via (B 1). For example,

the variance of $c_0'(\boldsymbol{x}, t)$ can be calculated by solving (6.1) for $c_0'(\boldsymbol{x}, t)$, squaring both sides and taking the phase-average, resulting in

$$\langle {c_0'}^2 \rangle_\phi = \left\langle \frac{1}{c_\infty^2(t)} \langle c(\boldsymbol{x}, t)^2 \rangle_{xz} \right\rangle_\phi + [c_0(y) + \widetilde{c}_0(y, \phi)]^2 - 2[\widetilde{c}_0(y, \phi) + c_0(y)] \left\langle \frac{1}{c_\infty(t)} \langle c(\boldsymbol{x}, t) \rangle_{xz} \right\rangle_\phi . \tag{B 2}$$

The statistically periodic turbulent flux can, also, be more simply extracted by multiplying both sides of (B 1) by $v'(\boldsymbol{x}, t)$, taking the plane average, and, finally, the phase average, resulting in

$$\langle v' c_0' \rangle_\phi = \left\langle \frac{\langle v'(\boldsymbol{x}, t) c(\boldsymbol{x}, t) \rangle_{xz}}{c_\infty(t)} \right\rangle_\phi , \tag{B 3}$$

where $\langle v'(\boldsymbol{x}, t) \rangle_{xz}$ vanishes at every time due to continuity and the no-slip conditions at the bottom wall.

Other important components of the scalar variance budgets can be calculated in the same way, such as the turbulent diffusion of scalar variance

$$\left\langle v' \frac{1}{2} {c_0'}^2 \right\rangle_\phi = \frac{1}{2} \left\langle \frac{1}{{c_\infty(t)}^2} \langle v' c^2(\boldsymbol{x}, t) \rangle_{xz} \right\rangle_\phi - \left[\widetilde{c}_0(y, \phi) + c_0(y)\right] \left\langle \frac{1}{c_\infty(t)} \langle v' c(\boldsymbol{x}, t) \rangle_{xz} \right\rangle_\phi \tag{B 4}$$

and the molecular diffusion and dissipation term

$$\langle c_0' \nabla^2 c_0' \rangle_\phi = \left\langle \frac{1}{c_\infty^2(t)} \langle c \nabla^2 c \rangle_{xz} \right\rangle_\phi - (\widetilde{c}_0(y, \phi) + c_0(y)) \left\langle \frac{\langle \nabla^2 c \rangle_{xz}}{c_\infty(t)} \right\rangle_\phi - \frac{\mathrm{d}^2}{\mathrm{d}y^2} \left[c_0(y) + \widetilde{c}_0(y, \phi)\right] \left\langle \frac{\langle c \rangle_{xz}}{c_\infty(t)} \right\rangle_\phi + (\widetilde{c}_0(y, \phi) + c_0(y)) \frac{\mathrm{d}^2}{\mathrm{d}y^2} (\widetilde{c}_0(y, \phi) + c_0(y)) . \tag{B 5}$$

## REFERENCES


AKHAVAN, R., KAMM, R. D. & SHAPIRO, A. H. 1991*a* An investigation of transition to turbulence in bounded oscillatory stokes flows. Part 1. Experiments. *J. Fluid Mech.* **225**, 395–422.

AKHAVAN, R., KAMM, R. D. & SHAPIRO, A. H. 1991*b* An investigation of transition to turbulence in bounded oscillatory Stokes flows. Part 2. Numerical simulations. *J. Fluid Mech.* **225**, 423–444.

ANTONIA, RA & ORLANDI, P. 2003 Effect of Schmidt number on small-scale passive scalar turbulence. *Appl. Mech. Rev.* **56** (6), 615–632.

BERGANT, R. & TISELJ, I. 2007 Near-wall passive scalar transport at high Prandtl numbers. *Phys. Fluids* **19**, 065105.

BOUDREAU, B. P. & JØRGENSEN, B. B. 2001 *The Benthic Boundary Layer: Transport Processes and Biogeochemistry*. Oxford University Press.

BOULDIN, D. R. 1968 Models for describing the diffusion of oxygen and other mobile constituents across the mud-water interface. *J. Ecol.* **56** (1), 77–87.

BRYANT, L. D., LORRAI, C., MCGINNIS, D. F., BRAND, A., WÜEST, A. & LITTLE, J. C. 2010 Variable sediment oxygen uptake in response to dynamic forcing. *Limnol. Oceanogr.* **55** (2), 950–964.

BURNS, N. M. & ROSS, C. 1972 Oxygen-nutrient relationships within the Central Basin of Lake Erie. Paper no. 6. USEPA *Tech. Rep.* TS-05-71-208-24. Canada Centre for Inland Waters, Burlington, Ontario.

CALMET, I. & MAGNAUDET, J. 1997 Large-eddy simulation of high-Schmidt-number mass transfer in a turbulent channel flow. *Phys. Fluids* **9**, 438–455.

CAMPBELL, J. A. & HANRATTY, T. J. 1983 Turbulent velocity fluctuations that control mass transfer to a solid boundary. *AIChE J.* **29** (2), 215–221.

COMMITTEE ON ENVIRONMENT AND NATURAL RESOURCES 2010 Scientific assessment of hypoxia in US coastal waters. *Tech. Rep.* Interagency Working Group on Harmful Algal Blooms, Hypoxia, and Human Health of the Joint Subcommittee on Ocean Science and Technology, Washington, DC.

COSTAMAGNA, P., VITTORI, G. & BLONDEAUX, P. 2003 Coherent structures in oscillatory boundary layers. *J. Fluid Mech.* **474**, 1–33.

DIAZ, R. J. & ROSENBERG, R. 2008 Spreading dead zones and consequences for marine ecosystems. *Science* **321** (5891), 926–929.

GAYEN, B., SARKAR, S. & TAYLOR, J. R. 2010 Large eddy simulation of a stratified boundary layer under an oscillatory current. *J. Fluid Mech.* **643**, 233–266.

GERMANO, M., PIOMELLI, U., MOIN, P. & CABOT, W. H. 1991 A dynamic subgrid-scale eddy viscosity model. *Phys. Fluids* A **3**, 1760–1765.

HANES, N. BRUCE & IRVINE, ROBERT L. 1968 New technique for measuring oxygen uptake rates of benthal systems. *J. (Water Pollut. Control Fed.)* **40** (2), 223–232.

HANRATTY, T. J. 1956 Turbulent exchange of mass and momentum with a boundary. *AIChE J.* **2** (3), 359–362.

HIGASHINO, M., CLARK, J. J. & STEFAN, H. G. 2009 Pore water flow due to near-bed turbulence and associated solute transfer in a stream or lake sediment bed. *Water Resour. Res.* **45** (12), W12414.

HIGASHINO, M., O'CONNOR, B. L., HONDZO, M. & STEFAN, H. G. 2008 Oxygen transfer from flowing water to microbes in an organic sediment bed. *Hydrobiologia* **614**, 219–231.

HIGASHINO, M. & STEFAN, H. G. 2011 Dissolved oxygen demand at the sediment–water interface of a stream: near-bed turbulence and pore water flow effects. *J. Environ. Engng* **137** (7), 531.

HINO, M., KASHIWAYANAGI, M., NAKAYAMA, A. & HARA, T. 1983 Experiments on the turbulence statitistics and the structure of a reciprocating oscillatory flow. *J. Fluid Mech.* **131**, 363–400.

JENSEN, B. L., SUMER, B. M. & FREDSØE, J. 1989 Turbulent oscillatory boundary layers at high Reynolds numbers. *J. Fluid Mech.* **206**, 265–297.

JIMÉNEZ, J. & MOIN, P. 1991 The minimal flow unit in near-wall turbulence. *J. Fluid Mech.* **225**, 213–240.

JIMENEZ, J. & PINELLI, A. 1999 The autonomous cycle of near-wall turbulence. *J. Fluid Mech.* **389**, 335–359.

KEATING, A., PIOMELLI, U., BREMHORST, K. & NEŠIĆ, S. 2004 Large-eddy simulation of heat transfer downstream of a backward-facing step. *J. Turbul.* **5** (20), 1–27.

LILLY, D. K. 1992 A proposed modification of the Germano subgrid-scale closure method. *Phys. Fluids* A **4**, 633–635.

LORKE, A., MÜLLER, B., MAERKI, M. & WÜEST, A. 2003 Breathing sediments: the control of diffusive transport across the sediment–water interface by periodic boundary-layer turbulence. *Limnol. Oceanogr.* **48** (6), 2077–2085.

MOSER, R. D., KIM, J. & MANSOUR, N. N. 1999 Direct numerical simulation of turbulent channel flow up to $Re = 590$. *Phys. Fluids* **11**, 943–945.

NA, Y. 2004 On the large-eddy simulation of high Prandtl number scalar transport using dynamic subgrid-scale model. *J. Mech. Sci. Technol.* **18** (1), 173–182.

O'CONNOR, B. L. & HONDZO, M. 2007 Enhancement and inhibition of denitrification by fluid-flow and dissolved oxygen flux to stream sediments. *Environ. Sci. Technol.* **42** (1), 119–125.

O'CONNOR, B. L. & HONDZO, M. 2008 Dissolved oxygen transfer to sediments by sweep and eject motions in aquatic environments. *Limnol. Oceanogr.* **53** (2), 566–578.

PATTERSON, J. C., ALLANSON, B. R. & IVEY, G. N. 1985 A dissolved oxygen budget model for Lake Erie in summer. *Freshwat. Biol.* **15**, 683–694.

PINCZEWSKI, W. V. & SIDEMAN, S. 1974 A model for mass (heat) transfer in turbulent tube flow. Moderate and high Schmidt (Prandtl) numbers. *Chem. Engng Sci.* **29** (9), 1969–1976.

POPE, S. B. 2000 *Turbulent Flows*. Cambridge University Press.

RABALAIS, N. N., DIAZ, R. J., LEVIN, L. A., TURNER, R. E., GILBERT, D. & ZHANG, J. 2010 Dynamics and distribution of natural and human-caused hypoxia. *Biogeosciences* **7** (2), 585–619.

RAO, Y. R., HAWLEY, N., CHARLTON, M. N. & SCHERTZER, W. M. 2008 Physical processes and hypoxia in the central basin of Lake Erie. *Limnol. Oceanogr.* **53** (5), 2007–2020.

RØY, H., HUETTEL, M. & JOERGENSEN, B. B. 2004 Transmission of oxygen concentration fluctuations through the diffusive boundary layer overlying aquatic sediments. *Limnol. Oceanogr.* **49** (3), 686–692.

SALON, S., ARMENIO, V. & CRISE, A. 2007 A numerical investigation of the stokes boundary layer in the turbulent regime. *J. Fluid Mech.* **570**, 253–296.

SCALO, C., BOEGMAN, L. & PIOMELLI, U. 2013 Large eddy simulation and low-order modelling of sediment oxygen uptake in a transitional oscillatory flow. *J. Geophys. Res.* **118** (1–14).

SCALO, C., PIOMELLI, U. & BOEGMAN, L. 2012*a* High-Schmidt-number mass transport mechanisms from a turbulent flow to absorbing sediments. *Phys. Fluids* **24** (8), 085103.

SCALO, C., PIOMELLI, U. & BOEGMAN, L. 2012*b* Large-eddy simulation of oxygen transfer to organic sediment beds. *J. Geophys. Res.* **117** (C6), C06005.

SHAW, D. A. & HANRATTY, T. J. 1977 Turbulent mass transfer to a wall for large Schmidt numbers. *AIChE J.* **23** (1), 28–37.

SLEATH, J. F. A. 1987 Turbulent oscillatory flow over rough beds. *J. Fluid Mech.* **182**, 369–409.

SPALART, P. R. & BALDWIN, B. S. 1989 Direct simulation of a turbulent oscillating boundary layer. In *Turbulent Shear Flows* (ed. J. C. André *et al.*). vol. 6. pp. 417–440. Springer.

TROWBRIDGE, J. H. & AGRAWAL, Y. C. 1995 Glimpses of a wave boundary layer. *J. Geophys. Res.* **100** (C10), 20729–20743.

VEENSTRA, J. N. & NOLEN, S. L. 1991 In-Situ sediment oxygen demand in five Southwestern US lakes. *Water Res.* **25** (3), 351–354.

VERZICCO, R. & VITTORI, G. 1996 Direct simulation of transition in Stokes boundary layers. *Phys. Fluids* **8**, 1341.

VITTORI, G. & VERZICCO, R. 1998 Direct simulation of transition in an oscillatory boundary layer. *J. Fluid Mech.* **371**, 207–232.

WANG, L. & LU, X. 2004 An investigation of turbulent oscillatory heat transfer in channel flows by large eddy simulation. *Intl J. Heat Mass Transfer* **47** (10–11), 2161–2172.

WARHAFT, Z. 2000 Passive scalars in turbulent flows. *Annu. Rev. Fluid Mech.* **32**, 203–240.

ZANG, Y., STREET, R. L. & KOSEFF, J. R. 1993 A dynamic mixed subgrid-scale model and its application to turbulent recirculating flows. *Phys. Fluids* A **5**, 3186.